

Geochimica et Cosmochimica Acta
Deep learning model to predict the structure and properties of aluminosilicate glasses and melts
--Manuscript Draft--

Manuscript Number:	
Article Type:	Article
Keywords:	aluminosilicate melt, glass, machine learning, viscosity, thermodynamic properties, magma, volcanology
Corresponding Author:	Charles Le Losq, Ph. D. Institut de Physique du Globe de Paris Paris, FRANCE
First Author:	Charles Le Losq, Ph. D.
Order of Authors:	Charles Le Losq, Ph. D. Andrew Valentine, Ph.D. Bjorn O. Mysen, Ph.D. Daniel R. Neuville, Ph.D.
Abstract:	Aluminosilicate melts and glasses are of paramount importance for geo- and materials sciences. They include most magmas, and are used to produce a wide variety of everyday materials, from windows to smartphone displays . Despite this importance, no general model with which to predict the molecular structural, thermodynamic and viscous properties of aluminosilicate melts exists. To address this, we introduce a deep learning framework, 'i-Melt', which combines a deep artificial neural network with thermodynamic equations. It is trained to predict 19 different latent and observed properties of melts and glasses in the K ₂ O-Na ₂ O-Al ₂ O ₃ -SiO ₂ system, including configurational entropy, viscosity, optical refractive index, density, and Raman signals. Viscosity can be predicted in the 10 ⁰ -10 ¹⁵ log Pa·s range using five different theoretical frameworks (Adam-Gibbs, Free Volume, MYEGA, TVF, Avramov-Milchev). The precision is better than 0.4 log Pa·s on unseen data. Density and optical refractive index (through the Sellmeier equation) can be predicted with errors of 0.05 and 0.005, respectively. Raman spectra for K ₂ O-Na ₂ O-Al ₂ O ₃ -SiO ₂ glasses are also predicted, with a mean error of ~ 15 %. This relatively high error is due to the limited number of examples available for training. Latent variables can also be predicted with good precisions. For example, the glass transition temperature, T _g , can be predicted to within 16 K, while the melt configurational entropy at the glass transition can be predicted to within 0.8 mol ⁻¹ K ⁻¹ . i-Melt can be used as a tool to explore systematically how structural and thermodynamic variables vary together with changes in melt/glass composition, and how different variables are correlated. We further use the model to help the understanding of the apparent links between changes in the molecular structure of silicic rhyolite lava and the dynamics of silicic volcanic eruptions, such as those at Yellowstone (U.S.A.), for example. Our deep learning framework represents a new tool to help understand and link experimental data to theory, and to allow behaviours to be predicted across a variety of applications, from material sciences to geochemistry.
Suggested Reviewers:	Doris Möncke Alfred University moncke@alfred.edu This person is an expert in glass and melts. Paul Asimow Caltech: California Institute of Technology asimow@caltech.edu This person is an expert in geological melts Kathleen Richardson University of Central Florida

kcr@creol.ucf.edu
This person is expert in glass, glass structure, glass properties

Dominique de Ligny
Friedrich-Alexander-Universität Erlangen-Nürnberg Orthopädische Universitätsklinik:
Friedrich-Alexander-Universität Erlangen-Nürnberg Orthopadische Universitätsklinik
dominique.de.ligny@fau.de
This person is an expert in glass, thermodynamic modeling, melt structure and properties.

Guillermo Lopez-Reyes
Universidad de Valladolid
guillermo.lopez.reyes@cab.inta-csic.es
This person is expert in machine learning

Paris, 23 March 2021

Dear Editor,

We are pleased to hereby submit our manuscript entitled “Deep learning prediction of glass and melt properties” to *Geochimica Cosmochimica Acta*.

The properties of molten rocks and glasses are critical to many disciplines, including glass industry and Earth sciences. Of particular interest is the link between the chemical composition of such materials, their molecular structure and their physical properties. No general model allows predicting such a link. In particular, the complex non-linear variations of thermodynamic properties with melt composition, such as configurational entropy, have been proven to be extremely difficult to reproduce. Here, we show that physics-guided deep neural networks can predict such quantities for their use in thermodynamic equations. Not limited to this, the deep neural network can also predict physical glass properties like density or refractive index.

The deep learning framework we created and trained takes chemical composition inputs, and returns melt viscosity through five different theories (it is thus “trans-theoretical”), as well as properties such as glass transition temperature, configurational entropy, glass density, glass optical refractive index or even glass Raman spectra. After training, the deep learning framework allows a systematic exploration and quantification of the links between structure (as seen by Raman spectra), chemical composition and properties of two states of silicate materials : glasses and melts. As a demonstration, we applied this idea on alkali aluminosilicate melts, for which an extended experimental dataset of high quality is available. Albeit simple, the study of this system with the deep learning framework already allows addressing practical problems, such the relationship between the composition of silicic magmas and the eruptive dynamics of silicic volcanoes like Yellowstone (USA).

This study is considered of high interest to the diverse readers of *Geochimica Cosmochimica Acta* because of the importance of the deep learning framework for the systematic exploration, quantification and prediction of the properties of geologic melts. Beyond volcanology, this approach can be transposed to many different fields. We have provided suggestions for reviewers below. We hope that you will consider our manuscript for publication in *Science*.

On behalf of all the authors, Yours sincerely,

Charles Le Losq

Current affiliation and contact details:

Université de Paris, Institut de physique du globe de Paris
1 rue Jussieu
75005 Paris, France
E-mail: lelosq@ipgp.fr

We suggest Sung Keun Lee (Seoul National University), Marc Norman (Australian National University) and Georges Calas (IMPMC) as associate editors for this paper. We also suggest the following reviewers:

Doris Möncke (Alfred University) moncke@alfred.edu

Paul Asimow (Caltech) asimow@caltech.edu

Kathleen Richardson (University of Central Florida) kcr@creol.ucf.edu

Dominique de Ligny (Friedrich-Alexander Universität) dominique.de.ligny@fau.de

Guillermo Lopez-Reyes (Universidad de Valladolid) guillermo.lopez.reyes@cab.inta-CSIC.es

Because of existing conflicts of interests, we ask the editor not to send the manuscript in review to the following people:

Mike Toplis, Midi-Pyrenees Observatory, Toulouse
Daniele Giordano, Torino University, Torino
Don B. Dingwell & Kai Uwe Hess, LMU Munich

1 Deep learning model to predict the structure and properties of aluminosilicate glasses and

2 melts

3 Charles Le Losq^{1,2,3,*}, Andrew Valentine^{2,4}, Bjorn O. Mysen³, Daniel R. Neuville¹

*4 ¹Université de Paris, Institut de physique du globe de Paris, CNRS-UMR 7154, Paris 75005,
5 France*

² Research School of Earth Sciences, Australian National University, Canberra 2601, Australia

⁷ ³*Earth Planets Laboratory, Carnegie Institution for Science, Washington D.C. 20001, U.S.A.*

⁸ *⁴Department of Earth Sciences, Durham University, South Road, Durham, DH1 3LE, UK.*

⁹ *Correspondence to: lelosq@ipgp.fr

10

11 **Abstract**

12 Aluminosilicate melts and glasses are of paramount importance for geo- and materials sciences.
13 They include most magmas, and are used to produce a wide variety of everyday materials, from
14 windows to smartphone displays. Despite this importance, no general model with which to
15 predict the molecular structural, thermodynamic and viscous properties of aluminosilicate
16 melts exists. To address this, we introduce a deep learning framework, ‘i-Melt’, which
17 combines a deep artificial neural network with thermodynamic equations. It is trained to
18 predict 19 different latent and observed properties of melts and glasses in the $K_2O-Na_2O-Al_2O_3-$
19 SiO_2 system, including configurational entropy, viscosity, optical refractive index, density, and
20 Raman signals. Viscosity can be predicted in the 10^0-10^{15} log Pa·s range using five different
21 theoretical frameworks (Adam-Gibbs, Free Volume, MYEGA, TVF, Avramov-Milchev). The

22 precision is better than 0.4 log Pa·s on unseen data. Density and optical refractive index
23 (through the Sellmeier equation) can be predicted with errors of 0.05 and 0.005, respectively.
24 Raman spectra for K₂O-Na₂O-Al₂O₃-SiO₂ glasses are also predicted, with a mean error of ~ 15 %.
25 This relatively high error is due to the limited number of examples available for training. Latent
26 variables can also be predicted with good precisions. For example, the glass transition
27 temperature, T_g , can be predicted to within 16 K, while the melt configurational entropy at the
28 glass transition can be predicted to within 0.8 mol⁻¹ K⁻¹.

29 i-Melt can be used as a tool to explore systematically how structural and
30 thermodynamic variables vary together with changes in melt/glass composition, and how
31 different variables are correlated. We further use the model to help the understanding of the
32 apparent links between changes in the molecular structure of silicic rhyolite lava and the
33 dynamics of silicic volcanic eruptions, such as those at Yellowstone (U.S.A.), for example.

34 Our deep learning framework represents a new tool to help understand and link
35 experimental data to theory, and to allow behaviours to be predicted across a variety of
36 applications, from material sciences to geochemistry.

37

38 **1. Introduction**

39 How do molten silicates move? How do they exchange heat with other media? How do they
40 crystallize? Questions such as these underpin many practical problems, ranging from the
41 dynamics of volcanic eruptions (Dingwell, 1996) and the formation of igneous rocks (Bowen,
42 1928), to the manufacture of novel glass, glass-ceramic and ceramic materials, including the
43 development of enhanced technological glass materials suitable for smartphone screens

44 (Varshneya and Bihuniak, 2017). To address such questions, knowledge of melt and glass
45 physical properties, such as viscosity, heat capacity and entropy, is necessary. These properties,
46 in turn, ultimately are governed by the liquid's composition and, therefore, atomic/ionic
47 structure (see for reviews Le Losq et al., 2019b; Mysen and Richet, 2019). Some properties,
48 such as silicate melt and glass heat capacity, can be reasonably predicted with existing models
49 (e.g., see for heat capacity Stebbins et al., 1984; Richet and Bottinga, 1985; Richet, 1987;
50 Tangeman and Lange, 1998; Webb, 2008; Giordano and Russell, 2017). However, other
51 properties are more difficult to model. This includes viscosity, because of its complex
52 dependence on temperature and melt composition. Silicate melt viscosity variations with
53 temperature, T , are, in most cases, non-Arrhenian. At constant T , viscosity can exhibit large and
54 non-linear variations with changing melt composition, particularly if T is in the supercooled
55 temperature domain. This domain is located well below the liquidus, close to the glass
56 transition temperature, which separates melts from glasses. Such a situation is unfortunate
57 because viscosity is of great interest: it influences not only volcanic processes (Dingwell, 1996;
58 Papale, 1999; Gonnermann and Manga, 2013; Gonnermann, 2015; Cassidy et al., 2018), but
59 also glass-forming processes in the glass manufacturing industry.

60

61 Currently, predictions of a property such as viscosity rely on (i) empirical models, (ii)
62 thermodynamic models, or (iii) molecular dynamics (MD) simulations. Empirical models are
63 interpolative in nature, and bring no information about the links between structural,
64 thermodynamic and dynamic properties of silicate melts. They can be sufficiently precise

65 enough, and thus, can be very useful, to accurately predict some properties, such as the glass
66 and melt heat capacities (Stebbins et al., 1984; Richet and Bottinga, 1985; Richet, 1987;
67 Tangeman and Lange, 1998; Russell and Giordano, 2017). In the case of viscosity, empirical
68 models rely on empirical equations (Bottinga and Weill, 1972; Shaw, 1972; Persikov, 1991; Hess
69 and Dingwell, 1996; Hui and Zhang, 2007; Giordano et al., 2008; Duan, 2014), such as the
70 Arrhenius or the Tamman-Vogel-Fulcher (TVF) laws. In term of precision, these empirical
71 models usually claim errors of 0.6 log Pa·s or larger, but predictive uncertainties can reach
72 much higher values in practice (e.g., Robert et al., 2013; Le Losq and Neuville, 2013; Sehlke and
73 Whittington, 2016; Di Genova et al., 2017). They provide a practical way of making viscosity
74 predictions, but their usefulness is restricted by the chemical composition and temperature
75 range within which the models have been calibrated. In addition, these models do not provide
76 any further information about the flow process.

77 Thermodynamic models circumvent the short-comings of empirical models, particularly.
78 their interpolative nature and the lack of physical/thermodynamic background that prevents
79 one to understand the processes underlying melt flow. Initially, thermodynamic models for
80 viscosity were limited to mixtures of specific melts comprising only a few oxides (e.g., Richet,
81 1984; Hummel and Arndt, 1985; Neuville and Richet, 1991). Analogous attempts were made to
82 model other properties, such as the model of Mysen (1995) which calculates the
83 configurational heat capacity of silicate melts from their fractions of tetrahedral $\text{SiO}_4 Q^n$ units (Q
84 being a tetrahedral unit and n the number of bridging oxygen it carries; $4-n$ thus gives the
85 number of non-bridging oxygens). Recent works further leveraged the recent advances in our

86 knowledge of links between melt structure, thermodynamic properties and viscosity, to
87 construct more complex thermodynamic models of the properties of silicate melts, either
88 directly from the melt chemical composition or based on knowledge of their structure. For
89 example, Sehkle and Whittington (2016) proposed a model, based on the Adam-Gibbs theory of
90 relaxation processes (Adam and Gibbs, 1965, see section 2.5.2), to predict the viscosity of
91 tholeiitic melts with an average error of 0.13 log Pa·s, on the 10^0 - 10^{12} Pa·s range. Le Losq and
92 Neuville (2017) also proposed a model based on the Adam and Gibbs theory of relaxation
93 processes. Their model connects viscosity, heat capacity, configurational entropy, structure
94 and chemical composition for melts in the Na₂O-K₂O-SiO₂ system and allows viscosity
95 predictions with an average error lower than 0.2 log Pa·s on the 10^0 - 10^{12} Pa·s range. A third
96 example is the model proposed by Starodub et al. (2019). It combines an associate solution
97 model of melt structure with the Avramov-Milchev equation of viscous flow (Avramov and
98 Milchev, 1988; Avramov, 2011) to predict melt viscosity on the 10^0 - 10^{12} Pa·s range in the Na₂O-
99 K₂O-Al₂O₃-SiO₂ system.

100 Structure-thermodynamic models, like those discussed above, can be precise and
101 provide important information about the links between composition, structure and properties.
102 However, such models suffer from an important drawback: a good knowledge of melt structure
103 is required. While this can be achieved for silicate melts through, for instance, Nuclear
104 Magnetic Resonance (NMR) spectroscopy (e.g., Maekawa et al., 1991), such information is
105 difficult to obtain for aluminosilicate compositions. For example, in their study of the
106 repartition of Al between Q^n tetrahedral units, Mysen et al. (2003) modeled the ²⁹Si NMR

107 spectra of aluminosilicate glasses. Their results highlight the challenges of such modeling: the
108 numerous Al-Si interactions broaden the ^{29}Si NMR signals. Such problems make it difficult to
109 determine with confidence the Q^n speciation in Al-bearing silicate melts. Raman spectroscopy
110 may also be used (McMillan, 1984; Matson and Sharma, 1985; Merzbacher and White, 1991;
111 Mysen, 1999), as testified by successful results for alkali silicate and aluminosilicate glasses
112 (Mysen, 1990, 2007; Mysen and Frantz, 1992; Neuville and Mysen, 1996; Malfait et al., 2007;
113 Zakaznova-Herzog et al., 2007; Koroleva et al., 2013; Nesbitt et al., 2021). However, the
114 variations of the Raman peak cross sections, which are needed to convert Raman peak areas in
115 Q^n unit fractions, are not known as well as would be desired. Furthermore, the peak-fitting
116 protocols can be subject to discussion, as shown by a lack of consensus visible when comparing
117 different studies (e.g., compare the methods described in the studies of B. O. Mysen et al.,
118 1982; Mysen, 1990; You et al., 2005; Malfait, 2009; Le Losq and Neuville, 2013; Le Losq et al.,
119 2014; Bancroft et al., 2018; Nesbitt et al., 2019, 2021). In any case, models that only rely on Q^n
120 fractions are incomplete because many other structural details affect the properties of
121 aluminosilicate melts. These include, but are not limited to, changes in Al coordination with
122 composition, temperature and pressure (Stebbins et al., 2000, 2008; Toplis et al., 2000;
123 Allwardt et al., 2005a, b; Kiczenski et al., 2005; Neuville et al., 2007; Massiot et al., 2008; D. R.
124 Neuville et al., 2008; Le Losq et al., 2014; Morin et al., 2014; Drewitt et al., 2015), Al-Si ordering
125 between tetrahedral units (Lee and Stebbins, 1999; Lee, 2005; Lee et al., 2016; Allu et al., 2018),
126 or excess non-bridging oxygens (Stebbins and Xu, 1997; Stebbins et al., 1999; Oglesby et al.,
127 2002; Iuga et al., 2005; Thompson and Stebbins, 2011, 2012, 2013; Xiang et al., 2013). From the

128 above non-exhaustive depiction of the current state of our knowledge of melt structure, it
129 appears that our incomplete knowledge of the complex polyhedral melt/glass structure
130 currently limit the extension of thermodynamic models to multicomponent magmatic and
131 industrial melt/glass compositions.

132 MD simulation (Rapaport, 2004) is another pathway that allows us to infer the structure
133 and properties of complex melts. Such models bring important structural, dynamic and
134 thermodynamic information by simulating atomic movements over picosecond timescales
135 (Guillot and Sator, 2007; Vuilleumier et al., 2009; Bauchy et al., 2013; Wang et al., 2014; Dufils
136 et al., 2017). They provide models that can be used to assess how melt behaves at
137 temperatures typically higher than 2000 K, how atoms move and interact, and how this affects
138 their physical properties such as viscosity and density. While predictions are informative about
139 processes at super-liquidus conditions and can be useful for high-temperature applications
140 (e.g., in glass furnace or in planetary magma oceans), they are less helpful at lower
141 temperatures, for example in the 700 - 1300 °C temperature range typical of volcanic eruptions.
142 Furthermore, MD simulation simulates the system on very short timescales, of tens of
143 picoseconds at most for classical MD models, with even shorter timescales for *ab initio*
144 calculations. This is very far from glass-making conditions, and extremely far from
145 volcanological timescales which span a wide range, from minutes to several thousands of years,
146 and sometimes beyond.

147 From the above discussion, there is no general framework that links variations of
148 temperature (T), pressure (P), melt composition (x), structure and physical properties, in order

149 to perform accurate predictions of the melt properties of interest for volcanology and material
150 sciences. Here, we show that such a model can be derived by leveraging the use of physics-
151 guided neural networks (PGNN). The PGNNs combine physical equations with artificial neural
152 networks. This brings advantages in comparison to both traditional physical/thermodynamic
153 models and “pure” machine learning models. PGNNs leverage our current knowledge of
154 physical systems by integrating existing physical equations, but add the power of machine
155 learning to infer connections between variables not yet understood theoretically – for instance,
156 between glass chemical composition and configurational entropy. PGNNs have been successful
157 in many applications (Willard et al., 2020), including the analysis of seismic waveforms (Ren et
158 al., 2020) and lake temperature modeling (Karpatne et al., 2018). This has inspired recent
159 efforts to model the viscosity of ionic liquids with neural networks (Paduszyński and Domańska,
160 2014; Beckner et al., 2018). For silicate melts, Cassar (2020) recently proposed the ViscNet
161 model, a PGNN model that combines either the VFT or the MYEGA viscosity equations (see
162 section 2.5.2) with a neural network to perform viscosity predictions of silicate and
163 aluminosilicate melts. Such results are very encouraging and showcase the ability of PGNN to
164 provide pragmatic, practical models for property predictions.

165 Here, we go a step further by presenting a PGNN model that combines several physical
166 equations with a deep learning neural network (named i-Melt), and predict many different melt
167 and glass properties of interest for geology and industry, including melt viscosity and
168 configurational entropy, glass density, optical refractive index and Raman spectra. i-Melt is thus
169 a PGNN “multitask” model, which has the ability to predict different features/properties of the

170 same object: a silicate melt/glass. i-Melt was trained on melt and glass compositions in the K₂O-
171 Na₂O-Al₂O₃-SiO₂ system, for which a fairly complete, albeit sparse, experimental dataset is
172 available. In this system, i-Melt allows systematic exploration of the links between melt/glass
173 composition, structure and properties as it will be presented in the following.

174

175 **2. Methods**

176 **2.1 Experimental Design**

177 The development of the deep learning model requires the collection and compilation of
178 viscosity, density, refractive index data, and Raman spectra for glasses and melts in the K₂O-
179 Na₂O-Al₂O₃-SiO₂ quaternary system (Fig. 1). The viscosity of supercooled melts for peralkaline
180 compositions in this system is not well understood, and we conducted additional experiments
181 to complement the existing dataset. We further compiled existing data as specified below, prior
182 to developing the i-Melt framework in the Python programming language, by using the PyTorch
183 library. All codes and data necessary to reproduce this study can be accessed using Jupyter
184 Notebooks, available from Github at <https://github.com/charlesll/i-melt>.

185

186 **2.2 Datasets**

187 Existing Raman spectra and observations of optical refractive index, density and
188 viscosity of alkali aluminosilicate glasses were selected by hand via a review of the existing
189 literature. Validation of the accuracy of viscosity data across different studies is critical and was
190 checked on melt compositions including Na₂Si₃O₇, NaAlSi₃O₈ and NaAlSi₂O₆. We plotted all

191 together the literature data for such compositions, and observed the mean trend of these data.
192 Most data fall within 0.1 log Pa·s, forming a clear general trend. Published data with deviations
193 larger than 0.1 log Pa·s compared to this general trend were discarded. Density and refractive
194 index come from various publications, in particular from publications reviewed in Mazurin et al.
195 (1987). Raman spectra were published data from the IPGP and Carnegie Institution for Science
196 laboratories (see below for details). All the data and their sources are provided in the database
197 available in the software repository. We thus have four different streams of data:

198 - $D_{viscosity}$, the dataset of viscosity measurements, composed of $X_{viscosity}$ chemical composition
199 entries (mole fractions) as well as their associated temperatures (Kelvin) and $y_{viscosity}$
200 observations (log Pa·s);

201 - $D_{density}$, the dataset of density measurements, composed of $X_{density}$ chemical composition
202 entries (mole fractions) and $y_{density}$ observations (g cm^{-3});

203 - D_{Raman} , the dataset of Raman spectra, composed of X_{Raman} chemical composition entries
204 (mole fractions) and y_{Raman} spectra observations (min-max scaled Raman intensities);

205 - $D_{optical}$, the dataset of optical refractive index, composed of $X_{optical}$ chemical composition
206 entries (mole fractions) as well as their associated wavelength (μm) and $y_{refractive\ index}$
207 observations.

208 $D_{viscosity}$, $D_{density}$ and $D_{optical}$ cover an important part of the glass-forming domain of alkali
209 aluminosilicates (Fig. 1). These data were, thus, used to train the artificial neural network with a
210 “performance oriented” mindset, i.e. we want the model predictions to be as accurate as
211 possible. D_{Raman} covers a more limited set of compositions (Fig. 1). It was used as a way of

212 improving multitask learning as well as a way of introducing structural information in the deep
213 learning framework.

214

215 ***2.3 Sample synthesis and viscosity-density measurements***

216 To extend the viscosity dataset for peralkaline aluminosilicate melts, additional
217 compositions were synthesized at IPGP in Paris from reagent-grade K_2CO_3 , Na_2CO_3 , Al_2O_3 and
218 SiO_2 dried oxide powders, following the protocol described in Le Losq and Neuville (2013).
219 Viscosity and density measurements follow the protocol used in the Geomaterial laboratory at
220 IPGP (Neuville, 2006; Le Losq and Neuville, 2013; Le Losq et al., 2014). Chemical compositions
221 (Table 1) have been measured using a Cameca SX50 electron microprobe, with a 30 nA current,
222 $U = 30$ kV, and 5 seconds of counting. Beam-induced alkali loss was minimized by working with
223 a defocused beam that was moved continuously during the analysis. The mean and standard
224 deviation values reported in Table 1 are calculated from 10-20 individual measurements on
225 each sample. The corresponding viscosity measurements are provided in Table 2, and are
226 affected by an error lower or equal to 0.03 log Pa·s. All measured viscosities were Newtonian –
227 no dependence on the strain rate was observed.

228

229 ***2.4 Raman spectroscopy***

230 Raman spectra of silicate and aluminosilicate glasses acquired at IPGP (Paris, France)
231 were recorded using a T64000 Jobin-Yvon® Raman spectrometer equipped with a confocal
232 system, a 1024 charge-couple detector (CCD) cooled by liquid nitrogen and an Olympus®

233 microscope. The optimal spatial resolution allowed by the confocal system is 1-2 μm^2 with a
234 $\times 100$ Olympus[®] objective, and the spectral resolution is 0.7 cm^{-1} . A Coherent[®] laser 70-C5 Ar⁺,
235 having a wavelength of 488.1 or 514.532 nm, has been used as the excitation line. Unpolarized
236 Raman spectra that were excited with a laser power of 100-150 mW on the sample were
237 acquired between 20 and 1500 cm^{-1} on pieces of glass from the starting materials.

238 Additional Raman spectra acquired at the Geophysical Laboratory on glasses along the
239 Na₂Si₄O₉-Na₂(NaAl)₄O₉ and K₂Si₄O₉-K₂(KAl)₄O₉ joins, previously published in Mysen (1996, 1999),
240 were added to the database. Those spectra were acquired with a Dilor XY confocal microRaman
241 spectrometer equipped with a cryogenic Thompson Model 4000 CCD. The 488 nm line of a
242 SpectraPhysics model 2025 Ar⁺ laser operating at several hundred mW at the sample was used
243 for sample excitation.

244 Preprocessing of the spectra was kept to minimum: (i) a linear baseline was adjusted to
245 the minima in the 700-800 and 1200-1300 cm^{-1} portions of the spectra and then subtracted to
246 obtained baseline-corrected spectra, (ii) the spectra were then corrected for temperature and
247 excitation line effects (see details and references in Le Losq and Neuville, 2013; Le Losq et al.,
248 2014), and (iii) the spectra were normalised to their maximum intensity such that the intensity
249 in each spectrum varies between 0 and 1. Only signals in the 400-1250 cm^{-1} range were
250 retained as different spectra had different starting and ending Raman shift values. After pre-
251 processing, spectra were saved in a HDF5 file for their future use.

252

253 **2.5 Deep learning model**

254 2.5.1 Overview

255 The i-Melt framework (Fig. 2) combines a deep artificial neural network with various
256 dynamic and thermodynamic equations. This strategy allows the development of an intelligent
257 model that links different observables from the same object (melt/glass). The artificial neural
258 network is a feed forward network with multiple interconnected hidden layers (Murphy, 2012;
259 Goodfellow et al., 2016). It either predicts directly-observable glass properties including
260 density, refractive index and Raman spectra, or outputs the latent variables (such as
261 configurational entropy, S^{conf} , a property that reflects the melt structure) required to predict
262 properties such as melt viscosity through five theoretical and empirical equations commonly
263 used for reproducing experimentally-observed variations of silicate melt viscosity with
264 temperature: Adam-Gibbs, MYEGA, Avramov-Milchev, Tamman-Vogel-Fulcher and Free Volume
265 Theory. In the next section, we will present the possibility of performing such *trans-theoretical*
266 predictions, i.e. the ability to predict a given property using different theoretical/empirical
267 frameworks but a single, common artificial neural network. The network predicts, given melt
268 composition, the different parameters of the different theoretical/empirical equations, which,
269 in turn, provide different values of the desired property. This allows one to predict melt
270 viscosity using, for instance, the Adam-Gibbs or Free Volume equations depending on
271 preference, and to compare final predictions as well as observe the connection and correlation
272 between the different variables of the equations.

273

274 2.5.2 Trans-theoretical predictions

275 No consensus exists regarding a “best theory” to explain and reproduce the variations of
276 melt viscosity with parameters such as temperature, pressure or composition. Despite this lack
277 of consensus, some models may be preferred. For instance, the Adam-Gibbs theory (Adam and
278 Gibbs, 1965) has been particularly successful in reproducing relaxation and viscosity data of
279 silicate melts (Richet, 1984; Scherer, 1984; Neuville and Richet, 1991; Bottinga et al., 1995;
280 Bottinga and Richet, 1996). It assumes that liquid movements occur through cooperative
281 molecular re-arrangements; viscosity (η) can be expressed as a function of temperature (T) and
282 composition (x) via

$$283 \log\eta(T, x) = A_e(x) + \frac{B_e(x)}{T(S^{conf}(T_g, x) + \int_{T_g}^T C_p^{conf}(x)/TdT)}, \quad (1)$$

284 with A_e representing a high-temperature limit, B_e a term proportional to the energy barriers
285 opposed to molecular re-arrangements, and S^{conf} and C_p^{conf} the melt configurational entropy
286 and heat capacity, respectively. T_g is the glass transition temperature. Here, we adopt the
287 empirical definition of T_g as equal to the temperature for which $\eta = 10^{12}$ Pa·s, and the
288 associated melt relaxation time is of ~100 s. The T_g calculated from this definition agrees within
289 20-30 K with the T_g determined from calorimetric measurements (e.g., Russell and Giordano,
290 2017), which themselves depend on the cooling/heating rates during calorimetric
291 measurements. The adopted T_g definition is thus coherent for viscosity modeling, as T_g derived
292 from the viscosity data refers to the relaxed melt and its equilibrium structure.

293 Alternatively, one might adopt the Free Volume theory (Cohen and Grest, 1979, 1984),
 294 which states that melts present liquid-like and solid-like molecular cells, their mobility being
 295 ensured by atomic diffusivity within/between liquid-like cells. This takes the form

$$296 \quad \log\eta(T, x) = A_{FV}(x) + 2B_{FV}(x)/\left(T - T_{FV}(x) + \sqrt{\left((T - T_{FV}(x))^2 + C_{FV}(x)T\right)}\right), \quad (2)$$

297 with $A_{FV}(x)$ again representing the high-temperature limit, $B_{FV}(x)$ a constant that depends on
 298 the molecular volume, $C_{FV}(x)$ a constant that has a dimension of temperature and that should
 299 be positive, and $T_{FV}(x)$ a constant identified as the temperature at which continuity of liquid-
 300 like cells is reached.

301 Beyond the Free Volume and Adam-Gibbs models, many other theories have been
 302 proposed to describe the viscous flow of liquids. Among those, some are empirical like the
 303 Tamman-Vogel-Fulcher (TVF) equation:

$$304 \quad \log\eta(T, x) = A_{TVF}(x) + B_{TVF}/(T - T_{TVF}), \quad (3)$$

305 with A_{TVF} , B_{TVF} and T_{TVF} adjustable parameters. We can also cite the Avramov and Milchev
 306 (1988) (AM) model, or the MYEGA model (Mauro et al., 2009) that is derived from eq. 1. Both
 307 propose equations relating viscosity, temperature as well as $T_g(x)$ and $m(x)$, the glass transition
 308 temperature and the fragility (equal to the slope of the viscosity *versus* temperature curve at
 309 T_g) of a melt with composition x . The AM model is expressed as (Avramov, 2011):

$$310 \quad \log\eta(T, x) = A_{AM}(x) + (12 - A_{AM}(x))\left(T_g(x)/T\right)^{m(x)/(12 - A_{AM}(x))}, \quad (4)$$

311 with A_{AM} a pre-exponential terms proportional to $\log\eta(T \rightarrow \infty)$. Similarly, the MYEGA
312 equation takes the form:

313
$$\log\eta(T, x) = A_e(x) + (12 - A_e(x))(T_g(x)/T)e^{(m(x)/(12-A_e(x))-1)\left(\frac{T_g(x)}{T}-1\right)}, \quad (5)$$

314 with A_e a pre-exponential term proportional to $\log\eta(T \rightarrow \infty)$ that was taken as equal to that
315 in the Adam-Gibbs theory (eq. 1) because the MYEGA equation is a daughter product of the
316 Adam-Gibbs theory. Equations 3 to 5 remain empirical or semi-empirical because unlike the
317 Adam-Gibbs or Free Volume equations, these expressions are not expressed in terms of
318 measurable physical quantities, such as heat capacity, for example. However, they do model
319 the viscosity dependence on temperature very well.

320 While the equations presented above are popular for silicate melts, no over-riding
321 consensus exists towards any one model appropriate for all liquids. In fact, some of those
322 models rely on very different theoretical backgrounds. The i-Melt approach circumvents the
323 problem of choosing one particular theory by proposing a *trans-theoretical* approach. The
324 artificial neural network is trained to predict melt viscosity using all five theoretical/empirical
325 frameworks (eqs. 1-5). It provides optimal common values for parameters that appear in
326 multiple theories, such as the glass transition temperature T_g . As a result, it allows comparison
327 of viscosity predictions between the different theories, and observation of how parameters
328 from the different theories correlate with each other, potentially providing insight into physical
329 inter-relationships.

330

331 *2.5.3 Data preparation: Train-Validation-Testing split and standardisation*

332 If a model performs well when tested against the training dataset, but fails at making reliable
333 predictions on new, unseen datasets, it is said to be ‘overfitting’. This is a common problem
334 affecting machine learning models. Here, we deploy several strategies to mitigate it. First, we
335 monitor the phenomenon: the available datasets were split into three different, randomly
336 chosen *training*, *validation* and *testing* subsets (Fig. 1). During the training process, the *training*
337 subset was used for training the model while the *validation* subset was used for monitoring
338 overfit and to trigger early stopping. The latter method consists in stopping the training process
339 when the Root-Mean-Square-Error (RMSE), measured between predictions and observations,
340 on the validation data subset stops decreasing and starts diverging from that measured using
341 the training data subset. This allows stopping the training process before the over-fitting
342 phenomenon appears (Goodfellow et al., 2016). The final predictive abilities of the trained
343 neural networks were then evaluated using the entirely unseen *testing* data subset. In the
344 present study, the data were randomly separated by composition (Le Losq et al., 2019a) to
345 avoid the pitfall of having the same glass/melt composition in the different *training*, *validation*
346 and *testing* subsets (a phenomenon known as ‘data leakage’). While $D_{viscosity}$, $D_{optical}$ and $D_{density}$
347 were each separated in three splits following the above protocol (Fig. 1), D_{Raman} was divided in
348 only two *train* and *validation* subsets due to its small size. This is not problematic, because we
349 do not aim at precise predictions of Raman spectra but rather use this dataset as a way to
350 improve the predictive capacity of the trained neural network and to introduce structural
351 knowledge.

352 After train-validation-test splitting, an important step in any machine learning data
353 preprocessing is standardization of the data. In practice, appropriate data scaling is often
354 essential to obtaining good convergence within algorithms (Goodfellow et al., 2016). The goal
355 of re-scaling is to promote feature variations near unity and to ensure that all features have
356 comparable numerical ranges: failure to do so tends to lead to instabilities in the gradient back-
357 propagation process that is central to training neural networks. In the present study, we have
358 implemented a custom approach. All chemical compositions inputs are in mole fractions, which
359 corresponds to a modification of min-max (0-1) scaling. Raman spectra were normalised to be
360 between 0 and 1. Viscosity, density and refractive index were not scaled, as scaling the outputs
361 was not found to affect network convergence. However, when outputs are unscaled, it is
362 essential to initialise the bias of the output layer of the neural network to match the expected
363 range of the predictions to be made, as developed for (e.g.) Mixture Density Networks (Bishop,
364 2006). After pre-processing, the different scaled *training*, *validation* and *testing* data subsets
365 were saved in Hierarchical Data Format HDF5 files for their future use.

366

367 2.5.4 *i-Melt model technical implementation*

368 i-Melt is implemented in the Python programming language, using the Pytorch machine
369 learning library (Paszke et al., 2019). It takes four inputs: the mole fractions of the SiO₂, Al₂O₃,
370 Na₂O and K₂O components. These are fed into to a neural network composed of k hidden
371 layers, each one having a given number of activation units (a.k.a neurons). By changing the
372 number of activation units between different hidden layers in a single network, training

373 convergence or final predictive abilities were not improved. For simplicity, we, thus, chose to
374 keep the same number of activation units in the different hidden layers. Having explored
375 various alternatives, we adopted the now-popular rectifier function (Glorot et al., 2011) as the
376 activation function of activation units, so that an activation unit receiving input, x , returns
377 output $y = \max(0, x)$. The outputs of the hidden layers were finally fed into two output linear
378 layers. The first output layer returns vectors that are Raman spectra, calculated from the linear
379 sum of the last neural network hidden layer. The second output linear layer returns 16 different
380 values:

381 - the parameters A_e , A_{AM} , A_{FV} and A_{TVF} (eqs. 1 to 5), as well as the coefficients B_1 to B_3
382 and C_1 to C_3 of the Sellmeier equation (see eq. 6 below) for the calculation of the glass
383 refractive index n , are directly given by the linear outputs; and
384 - the natural logarithms of $S^{conf}(T_g)$, C_{FV} , T_g , T_{FV} , T_{TVF} , the melt fragility m , and the glass
385 density d .

386 The use of the logarithm in the latter case was inspired by a similar strategy proposed by Bishop
387 (2006) for Mixture Density Networks. It ensures that quantities are assigned positive values in
388 accordance with their physical meaning. We also found the use of logarithms to aid rapid
389 convergence during training. Other terms such B_e , B_{FV} and B_{TVF} were calculated from eqs. 1 and
390 5 and the knowledge of the other parameters.

391 Neural network predictions can be used in equations 1 to 5 to predict of melt viscosity.
392 The neural network also directly provides different observables such as glass density, glass

393 transition temperature or Raman spectra. Furthermore, the coefficients B_1 to B_3 and C_1 to C_3
394 are used to predict the refractive index at given wavelength, $n(\lambda)$, via the Sellmeier equation:

395
$$n(\lambda) = \sqrt{\left(1 + \frac{B_1 \times \lambda^2}{\lambda^2 - C_1} + \frac{B_2 \times \lambda^2}{\lambda^2 - C_2} + \frac{B_3 \times \lambda^2}{\lambda^2 - C_3}\right)} . \quad (6)$$

396 The artificial neural network allows us, therefore, to input chemical compositions and obtain
397 predictions for:

- 398 - melt viscosity, within five distinct theoretical or empirical frameworks,
399 - glass transition temperature,
400 - latent variables like configurational entropy and fragility,
401 - glass density,
402 - glass refractive index as a function of wavelength, and
403 - glass Raman spectra.

404 These predictions depend on a large number of tuneable parameters integral to the neural
405 network. During network training, the database of observed glass properties was used to
406 optimize these parameters, seeking values that enable good average predictive performance.

407

408 **2.5.4 Training i-Melt**

409 During training, we monitored the least-square deviations between measurements and
410 predictions for viscosity from eqs. 1 to 5 as well as density, optical refractive index and Raman
411 spectra. Loss functions were also added for known viscous T_g and $S^{conf}(T_g)$ values in the dataset
412 $D_{viscosity}$. This allowed better constraints on the estimates of $S^{conf}(T_g)$, a parameter that is difficult
413 to evaluate because strong correlations between B_e and $S^{conf}(T_g)$ prevent equation 1 from

414 having a non-ambiguous solution. This correlation originates from the involvement of the
415 intrinsic entropy, S_c^* , of the molecular subunits involved in the melt viscous flow / relaxation
416 process in both B_e and $S^{conf}(T_g)$ (Adam and Gibbs, 1965; Toplis, 1998, 2001).

417 Batch training was performed using the Adam optimizer with a learning rate of 0.001,
418 and monitoring the global loss on the *training* and *validation* data subsets. Early stopping,
419 which consists of stopping the training process when the first signs of over-fitting are detected
420 (Goodfellow et al., 2016), was used to avoid overfitting: when the global loss function on the
421 *validation* data subset ceased to decrease for more than 50 epochs, training was halted and the
422 network exhibiting the best validation loss was saved. Dropout (Srivastava et al., 2014), a
423 method that entails randomly turning off a given fraction of activation units at each training
424 iteration, was also applied. This method is known to promote generalization and reduce
425 overfitting.

426

427 **3. Results**

428 **3.1 Optimization of the artificial neural network architecture**

429 The i-Melt framework uses a feed-forward deep neural network (Fig. 2). Such network
430 feeds its inputs to several fully connected hidden layers composed of a given number of
431 activation units, a.k.a. neurons or perceptrons. Before presenting any results regarding the
432 performance of the model, we first document the optimal architecture and the way we
433 searched for it. This optimal architecture is important as it determines its performance to fit the

434 existing data, its sensitivity to overfitting, and its generalization ability (i.e. its ability to provide
435 precise and accurate predictions for new, unseen compositions).

436 The architecture of the hidden layers was optimized via a random search process
437 (Bergstra and Bengio, 2012). How the number of hidden layers and that of hidden activation
438 units affected the neural network overall performance was monitored by training 3000 artificial
439 neural networks under the same conditions on the same datasets. During this process, the
440 dropout parameter, p , was also varied. This parameter represents the percent of neurons per
441 layer turned off at each training iteration (Srivastava et al., 2014). In parallel, training datasets
442 with different numbers of samples were also generated. This allowed observing how the
443 number of samples affects the training of a given neural network architecture. The neural
444 network performances were documented using the RMSE between viscosity data predictions
445 and measurements. The results of those tests are reported in figure 3.

446 Figure 3a reveals that the RMSE on the different training, validation and testing datasets
447 become constant with more than ~70 sample compositions. This implies that, in the quaternary
448 alkali aluminosilicate system examined here, data from at least 70 different chemical
449 compositions were necessary to train the model efficiently, i.e. to get a model providing good
450 predictions while avoiding overfitting.

451 Regarding the neural network architecture (Fig. 3b,c,d), the RMSE of the different data
452 subsets all converge to values of ~0.4 log Pa·s for moderately deep neural network with 3 to 5
453 layers and 200-300 units per layer. Therefore, best performance was, in general, reached with
454 more than 1000 neurons in total in the hidden layers (Fig. 3b). Those results indicate that

455 moderately deep neural network generalizes better than shallow ones on this problem with
456 small datasets. The dropout method helps slightly in preventing overfitting, but is not a critical
457 feature in the present case (Fig. 3e). It actually seems that low to very-low dropout values
458 should be preferred. The difference of the RMSE between the training, testing and validation
459 data subsets are lowest for $p < 0.1$.

460 From this random search, the 10 best neural networks with the lowest error on the
461 validation data subset were selected. Given the results presented in Fig. 3, overfitting by each
462 network should be very limited but may be still present. To limit this issue further, all reported
463 predictions by i-Melt were calculated from the average of those from the 10 best neural
464 networks. This method is called bagging (Breiman and Breiman, 1996) and promotes
465 generalization (good predictions on new samples) of machine learning algorithms. This,
466 combined with the developed training protocol (see above), allowed i-Melt to provide good
467 generalization abilities. Furthermore, multi-task learning is performed here, as the neural
468 network is trained to predict different features (properties like density or T_g , observables like
469 Raman spectra...) from the same objects. This helped further limiting overfitting because
470 artificial neural networks learning to predict multiple related features/observables tend to
471 show better prediction abilities compared to those trained to predict only a given
472 task/parameter/feature (Caruana, 1997). We observed this by performing a few tests, training a
473 few neural networks to only predict viscosity. Those resulted in RMSE of $\sim 0.5 - 0.6 \text{ log Pa}\cdot\text{s}$,
474 higher than those of neural networks trained to predict multiple properties (lower than 0.4 log
475 $\text{Pa}\cdot\text{s}$, see below).

476

477 **3.2 Melt and glass property predictions**

478 This overall training strategy results in i-Melt providing good predictions for unseen
479 samples from the testing data subsets not included in the training, despite our small
480 experimental datasets. Trans-theoretical predictions of η (Figs. 4, 5) are possible with good
481 precision. The RMSE values are lower than 0.4 log Pa·s on the testing data subset (Table 3). For
482 comparison, the RMSE of the best empirical magma viscosity models typically are higher than,
483 or equal to 0.6 log Pa·s (e.g. Giordano et al., 2008). Eqs. 1 to 5 all yield similar values (Fig. 5),
484 except at very low viscosities where predictions through the free volume theory or the TVF
485 equation seem affected by some bias in the training dataset. However, such bias is not
486 observed in the other validation and testing datasets. Overall, the most consistent predictions
487 appear to come from the Adam-Gibbs equation along with the related MYEGA and the
488 Avramov-Milchev models, with no systematic outliers visible in the RMSE histograms (Fig.
489 5a,c,d, iv).

490 The melt/glass properties are also well predicted by i-Melt. Known viscous T_g and
491 $S^{conf}(T_g)$ are predicted within 16 K and 0.8 J mol⁻¹ K⁻¹, respectively (Fig. 6a,b). The glass density
492 and refractive index are also predicted to within 0.05 g cm⁻³ and 0.005, respectively (Fig. 6c,d,
493 Table 3). For the two latter properties, a few outliers are visible and correspond to extreme
494 compositions along the SiO₂-Al₂O₃ join (Figs. 1c,d, 6c,d) for which only a few data points are
495 available. This is therefore unsurprising, particularly considering that there is large variations in
496 glass and melt properties along this join (e.g., Okuno et al., 2005; Ando et al., 2018).

497

498 **3.3 Structural information through Raman spectra predictions**

499 In addition to physical and thermodynamic properties, i-Melt has the ability to predict
500 structure-dependent features such as Raman spectra of glass. Considering the very small
501 experimental Raman dataset (Fig. 1b), global variations of Raman signals have been well-
502 captured (Fig. 4b, 6e) and can be predicted within ~18 % (average mean absolute deviation
503 between observed and predicted spectra from the validation data subset). i-Melt thus embeds
504 structural information, and allows estimation of structural parameters from Raman spectra,
505 including the ratio of intra- and inter-tetrahedral aluminosilicate vibrations, R_{Raman} . This ratio is
506 calculated from the integrals of Raman intensities I_R observed at the Raman shifts $\bar{\nu}_1, \bar{\nu}_2$, in two
507 regions: between 0 and 670 cm^{-1} , and between 800 and 1300 cm^{-1} . In other terms, we calculate
508 two areas under the curve, A_{LW} (integrated intensity in the $0\text{-}670\text{ cm}^{-1}$ range) and A_{HW}
509 (integrated intensity in the $800\text{-}1300\text{ cm}^{-1}$ range), and obtain R_{Raman} from their ratio:

510

511
$$R_{Raman} = \frac{A_{LW}}{A_{HW}} . \quad (7)$$

512

513 A_{LW} integrates the signals assigned to bending/stretching of Q^n - Q^n intertetrahedral vibrations in
514 the glass network (Bell et al., 1968; Sen and Thorpe, 1977; Furukawa et al., 1981; McMillan,
515 1984), and A_{HW} those assigned to stretching of Al-O and Si-O bonds in Q^n units (Brawer and
516 White, 1975, 1977; Virgo et al., 1980; Furukawa et al., 1981; Mysen et al., 1982; McMillan,
517 1984). The integration boundaries were selected by observing all the spectra plotted together.

518 They correspond to common limits that delimitate the frequencies of the inter-tetrahedral Q^n -
519 Q^n and intra-tetrahedral Q^n vibrational regions. While some small changes could be made in
520 some cases, our selection of common boundaries for all glass Raman spectra robustly captures
521 the general trend.

522 The addition of network modifier metal cations to silica glass is accompanied by
523 increases in the fractions of depolymerized Q^n units (like Q^2 and Q^3 units) and, in parallel, by an
524 increase of the number of non-bridging oxygens per tetrahedral unit (NBO/T, see Mysen et al.,
525 1982). This results in a large decrease in the ratio R_{Raman} (Giordano and Russell, 2018). R_{Raman}
526 thus can serve as a measure of the glass $\text{SiO}_2\text{-AlO}_2$ network connectivity and topology: the
527 higher R_{Raman} is, the higher the aluminosilicate network connectivity, the lower the NBO/T.
528 Because of such link, R_{Raman} is linked to variations in melt properties, as confirmed by the study
529 of Giordano and Russell (2018). i-Melt can predict R_{Raman} within 15 %. There is a strong data gap
530 for R_{Raman} between ~ 2 and ~ 4 (value corresponding to that of silica glass) because there are very
531 few Raman spectra in the dataset at SiO_2 concentrations above ~ 90 mol%, and, above such
532 concentration, R_{Raman} varies strongly with silica content. Consequently, only one spectrum (that
533 of silica) constrains the model at very high R_{Raman} values. This data gap originates from the
534 difficulty to obtaining samples above ~ 90 mol% SiO_2 . At such high silica concentrations,
535 unmixing can happen during quench for $\text{Na}_2\text{O}\text{-SiO}_2$ compositions (e.g., Jarry and Richet, 2001).
536 In addition, high liquidus temperatures make the synthesis of glasses difficult for Al-bearing
537 compositions (Schairer and Bowen, 1955, 1956). Nevertheless, information from new
538 experiments in silica-rich melts could be important to bring information to the model about

539 melt/glass structural behavior between an extreme composition like SiO₂ and multicomponent
540 melts/glasses.

541

542 **3.4 Model internal consistency**

543 The ability to predict the melt fragility, m , permits further testing of the internal
544 consistency of i-Melt. Indeed, experimental data indicate that a direct correlation between m
545 and the ratio of the configurational heat capacity at T_g over the configurational entropy at the
546 glass transition, $C_p^{conf}(T_g)/S^{conf}(T_g)$, exists (Webb, 2008; Russell and Giordano, 2017). This is
547 predicted by the Adam and Gibbs theory because (Toplis et al., 1997a):

548
$$m = \frac{B_e}{S^{conf}(T_g)T_g} \left[1 + \frac{C_p^{conf}(T_g)}{S^{conf}(T_g)} \right]. \quad (8)$$

549 i-Melt predicts this correlation (Fig. 7). The model is, thus, internally consistent because it
550 respects the correlation expected from eq. 8. The model predictions fall between the trends
551 found by the experimental studies of Russell and Giordano (2017) and Webb (2008). The results
552 of those studies predicted a good correlation between m and $C_p^{conf}(T_g)/S^{conf}(T_g)$. Here, some
553 scatter is visible. It most probably arises from the propagation of the uncertainties affecting the
554 different predicted values. The m and $S^{conf}(T_g)$ predictions are affected by uncertainties, as well
555 as the melt and glass C_p calculations. Indeed, i-Melt internally calculates $C_p^{conf}(T_g)$ as $C_p^{liquid}(T_g) -$
556 $C_p^{glass}(T_g)$, with $C_p^{liquid}(T_g)$ predicted from the model of Richet and Bottinga (1985) and $C_p^{glass}(T_g)$
557 calculated from the Dulong-Petit limit of 3R, with R the perfect gas constant. Those $C_p^{liquid}(T_g)$
558 and $C_p^{glass}(T_g)$ calculations are also affected by uncertainties. The combination and propagation

559 of all those sources of uncertainties thus probably explains the greater scatter observed in
560 Figure 7 compared to experimental studies (Webb, 2008; Russell and Giordano, 2017). Finally,
561 some outliers are also visible, and correspond to compositions mostly on the SiO₂-Al₂O₃ join.
562 Along this binary, no supercooled viscosity data are available to constrain the melt fragility, and
563 melt/glass C_p predictions probably are affected by important errors. The combination of those
564 two problems probably explains the occurrence of the observed outliers.

565

566 **4. Discussion**

567 The deep learning framework offers opportunities to explore objectively the links
568 between chemical, structural, thermodynamic and dynamic parameters of materials. Beyond
569 this, the framework allows systematic predictions of melt and glass properties that can be of
570 use to address problems in volcanology, such as the link between lava composition and the
571 dynamics of eruptions, or other fields. Below, we will develop a few examples showcasing the
572 information that can be obtained from the deep learning framework.

573

574 **4.1 Exploration of composition-structure-property links**

575 i-Melt allows a systematic exploration of the links between different observed and
576 latent variables. This allows investigating the contributions of topological (i.e., the geometry and
577 interconnectivity of the T-O-T network, with T= Si,Al) and chemical effects (i.e., effects resulting
578 from mixing different cations in similar sites) to different properties. For example, R_{Raman} , and,

579 therefore, the glass network topology correlates with the glass transition temperature (Fig. 8a).
580 It also correlates with quantities proportional to energy barriers opposed to ionic mobility in
581 melts like the B_{FV} term of the Free Volume viscosity equation (Fig. 8b, eq. 2). This result agrees
582 very well with the general knowledge of the influence of the topology/connectivity of the
583 aluminosilicate network on melt transport properties (e.g., Bockris et al., 1955; Mysen et al.,
584 1980; Mysen, 1991).

585 However, the correlation between R_{Raman} and glass transition temperature T_g is not
586 perfect. Some influence of the glass composition on the R_{Raman} versus T_g relationship is visible in
587 figure 8a. It probably originates from metal cation chemical mixing effects that can affect T_g
588 (Isard, 1969; Day, 1976). Indeed, while cationic mixing effects influences only slightly properties
589 directly linked to the aluminosilicate network connectivity (Le Losq and Neuville, 2017), they
590 strongly affect properties such as $S^{conf}(T_g)$ that is influenced by cationic / molecular interactions
591 and steric hindrance effects (Richet, 1984; Hummel and Arndt, 1985; Neuville and Richet, 1991;
592 Neuville and Mysen, 1996; Maehara et al., 2005; Goldstein, 2011). This agrees with predictions
593 for $S^{conf}(T_g)$. The results in figure 8c show a clear effect of melt composition on the $S^{conf}(T_g)$
594 versus R_{Raman} relationship. Such chemical effects also affect C_{FV} (eq. 2, Fig. 8d). This latter term
595 encompasses local cationic influences on melt free volumes in the Free Volume theory (Cohen
596 and Grest, 1979). As a result, it can be expected that mixing different cations will affect this
597 term, explaining the observation made in figure 8d. Results actually suggest a link between C_{FV}
598 and $S^{conf}(T_g)$, as corroborated by a Spearman correlation coefficient of 0.93 between the two
599 variables.

600 Other properties show interesting correlations. Figure 9 shows the Spearman
601 correlation coefficients, r_s , between the different variables/properties predicted by the deep
602 learning framework. We observe high correlations between the parameters of the Free Volume
603 and the TVF equations. For example, B_{FV} and B_{TVF} are highly correlated ($r_s = 0.995$). While B_e is
604 not strongly correlated with the latter variables, the ratio $B_e/S^{conf}(T_g)$ is ($r_s = 0.996$ and 0.999
605 with B_{FV} and B_{TVF} , respectively). B_{FV} and B_{TVF} play the role of some kind of activation energies in
606 eqs. 2 and 3. They thus are related to the energy barriers opposed to the molecular movements
607 at the root of viscous flow. The ratio $B_e/S^{conf}(T_g)$ also is related to those energy barriers (see
608 below, eqs. 9, 10). The strong correlations between R_{Raman} and $B_e/S^{conf}(T_g)$, B_{FV} and B_{TVF} (Fig. 9)
609 thus indicates that the SiO₂-Al₂O₃ aluminosilicate network connectivity and topology mostly
610 controls those energy barriers. This may explain the correlation between the network topology
611 as quantified by R_{Raman} and the glass transition temperature of alkali aluminosilicate melts,
612 discussed previously (Figs. 8, 9).

613 Properties at the denominator in eqs. 1 to 5 show more complex correlations among
614 themselves, and with other variables (Fig. 9). A generally strong correlation is observed
615 between variables at the denominator of eqs. 1 to 5 and the pre-exponential terms reflecting
616 high temperature viscosity limits, namely A_{TVF} , A_{AM} , A_{FV} and A_e (Fig. 9). For example, $r_s = -0.93$
617 for the correlation between $S^{conf}(T_g)$ and A_e , $r_s = -0.981$ for the correlation between C_{TVF} and
618 A_{TVF} , and $r_s = 0.94$ for that between A_{AM} and the fragility, m . This reflects a numerical correlation
619 between the pre-exponential terms and the denominators of viscosity equations 1-5. A way to
620 avoid such correlations, which can bias calculations, is to set the A_{TVF} , A_{AM} , A_{FV} and A_e pre-

621 exponential terms to composition-independent values. Such practice agrees with the general
622 idea that there is a common high temperature viscosity limit (Persikov, 1991; Russell et al.,
623 2003; Giordano et al., 2008; Russell and Giordano, 2017). However, this can be questioned for
624 alkali aluminosilicate melts. Indeed, the study of Robert et al. (2019) suggests that, for alkali
625 tectosilicate melts, A_e could vary as a function of the melt Al/Si ratio. This agrees with earlier
626 findings of Toplis (1998), who showed that A_e actually varies as a function of the ratio $B_e/(Al+Si)$
627 for various alkali and alkaline earth melt compositions. In the present model, A_{TVF} , A_e , A_{FV} or A_{AM}
628 are allowed to vary with melt composition, such that we can check if the model corroborate the
629 findings of Robert et al. (2019) and Toplis (1998). In Figure 10a, we observe that, for
630 compositions covering a wide compositional field of the glass forming domain (see inset in Fig.
631 10b), values of A_e range between ~ -1.0 and $\sim -2.5 \log Pa\cdot s$, those of A_{FV} between ~ -2.0 and $\sim -$
632 $3.5 \log Pa\cdot s$, those of A_{AM} between ~ -0.2 and $\sim -1.0 \log Pa\cdot s$, and those of A_{TVF} between ~ -6.0
633 and $-4.0 \log Pa\cdot s$. The distributions of those parameters are asymmetric and complex. A_e and
634 A_{TVF} clearly are trimodal, while A_{FV} and A_{AM} distributions are asymmetric and present sharp
635 terminations on one of their side. This suggests the existence of complex compositional effects.
636 Fig. 10b corroborates this idea, and actually the findings of Robert et al. (2019). There is a
637 general effect of the melt Al/Si ratio on the value of A_e . A_{FV} also shown variations that correlate,
638 albeit in a complex manner, with Al/Si, while A_{AM} do not show systematic variations with Al/Si
639 (not shown). Those results thus corroborate the suggestion that for melts in ternary and
640 quaternary systems, the pre-exponential terms in eqs. 1 and 2 may slightly depend on
641 compositions, and particularly on the Al and Si concentrations and ratios.

642

643 **4.2 Links between the Adam-Gibbs and the Free Volume theories**

644 The above analysis highlighted important correlations between variables from different
645 theories (Fig. 9). The trans-theoretical character of i-Melt allows us to go further: it allows
646 systematic inference for a given property using different theories, and observation of the
647 relationship between the latent variables of these theories. For example, one might explore the
648 links between the Adam-Gibbs and Free Volume theories, and, thus, test the proposition of
649 Hodge (1994) of building a Free Volume version of the Adam-Gibbs theory.

650 In the Free Volume theory, solid-like and liquid-like molecular cells are distinguished and
651 separated by a critical volume, v^* . Viscous flow occurs via cooperative molecular movements
652 between liquid-like cells. In the Adam-Gibbs theory, viscous flow occurs via cooperative
653 motions of molecular segments of a size $z^*(T)$, characterized by an intrinsic entropy S_c^* . The two
654 theories thus share common philosophical underpinnings, including the important assumption
655 that viscous flow occurs via cooperative movements of molecular entities in the melt. This
656 relationship can be recognized upon consideration of the parameters of eqs. 1 and 2. Indeed,
657 B_{FV} embeds some structural information because it depends on v^* :

658
$$B_{FV} = v^* z_o, \quad (9)$$

659 where z_o is an adjustable parameter. Similarly, the ratio $B_e/S^{conf}(T_g)$ embeds molecular subunit
660 length-scale information as (Toplis, 1998)

661
$$B_e/S^{conf}(T_g) = [\Delta\mu z^*(T_g)]/R, \quad (10)$$

662 with $\Delta\mu$ the energy barriers opposed to the rearrangement of molecular subunits of size $z^*(T_g)$,
663 and R the perfect gas constant. We can consider v^* and z^* as structural parameters embedding
664 information about the volume or length-scale of the cooperative molecular regions. Therefore,
665 these parameters should both depend on melt or glass structure. This is confirmed by the fact
666 that both B_{FV} and $B_e/S^{conf}(T_g)$ correlate very well with R_{Raman} ($r_s = 0.991$ and 0.988 , respectively,
667 see details in section 4.1 and also Fig. 9). This finding supports the idea that it should be
668 possible to develop a Free Volume version of the Adam-Gibbs theory (Hodge, 1994; Liu et al.,
669 2015). More generally, the links between B_{FV} , $B_e/S^{conf}(T_g)$ and R_{Raman} support the general
670 hypothesis that melt viscous flow occurs when a critical molecular length-scale is reached. This
671 length-scale can be indirectly observed through Raman signals (Fig. 8b) and strongly influences
672 the glass transition temperature T_g (Fig. 8a).

673

674 **4.3 Configurational entropy of alkali aluminosilicate melts**

675 In section 4.1, it was highlighted that cationic mixing results in excess entropy and
676 influences, therefore, variables such as $S^{conf}(T_g)$, leading to its complex dependence on melt
677 composition and structure (Fig. 8c). Mixing between two cations in silicate and aluminosilicate
678 melts can be random (Neuville and Richet, 1991; Neuville and Mysen, 1996) or not (Seifert et
679 al., 1982; Lee, 2005; Neuville, 2006; Le Losq and Neuville, 2013, 2017; Robert et al., 2019). It
680 can occur between Si and Al “network formers” (Neuville and Mysen, 1996), between “network
681 modifier” metal cations (Richet, 1984; Neuville and Richet, 1991; Lee et al., 2003) or between
682 the “charge compensator” metal cations that compensate the electrical charge deficit of AlO_4^-

units in aluminosilicate compositions (e.g., Neuville and Richet, 1991; Robert et al., 2019). Such mixing effects usually are difficult to predict, and subject to interpretation. i-Melt helps solving this problem by enabling systematic quantification and visualization of such phenomena. For example, as seen in Figure 11, $S^{conf}(T_g)$ displays systematic variations as a function of the chemical composition of alkali aluminosilicate melts. Increasing Al concentration leads to decreasing $S^{conf}(T_g)$ (Fig. 11a,b). The Al/(Na+K) ratio also largely affects the way Na and K mix. Without Al, their interaction results in an entropy excess (Fig. 11c) and, hence, in decreases in melt viscosity because viscosity is proportional to the inverse of $S^{conf}(T_g)$ (eq. 1). This pattern changes with increasing Al/(Na+K), because as Al is introduced into the glass network, the role of alkali metals changes (see chapters 4 and 8 of Mysen and Richet, 2019). In presence of Al, Na and K are present in different structural environments (McKeown et al., 1985; Jackson et al., 1987; Le Losq and Neuville, 2017), inducing less and less excess entropy of mixing as Al/(Na+K) increases (Le Losq et al., 2017; Robert et al., 2019). As a result, $S^{conf}(T_g)$ varies more and more linearly upon mixing Na and K (Fig. 11d,e,f). Finally, i-Melt predicts small $S^{conf}(T_g)$ values for K-rich and Al-rich melts (Fig. 11b,f), in agreement experimental findings (Richet and Bottinga, 1984; Le Losq and Neuville, 2013; Le Losq et al., 2017; Robert et al., 2019). This is explained by Al and K respectively promoting the polymerization of the melt network (decrease in NBO/T) and the formation of larger cooperative molecular domains involved in the melt viscous flow (e.g., Riebling, 1966; Taylor and Rindone, 1970; Rammensee and Fraser, 1982; Mysen, 1988; Toplis et al., 1997b; Mysen and Toplis, 2007; Xiang et al., 2013; Le Losq et al., 2017). The variations in $S^{conf}(T_g)$ with the composition of aluminosilicate melts, thus, depend mostly on (i)

704 how metal cations interact together, and (ii) on how those interactions are affected by the
705 presence of Al, and by Si-Al interactions.

706

707 **4.4 Melt fragility and model extrapolations**

708 Two of the selected viscosity equations (eqs. 4, 5) share melt fragility as a common
709 parameter in their expressions. Melt fragility is the slope of the viscosity *versus* T curve at T_g ,
710 and scales with the ratio between C_p^{conf} and S^{conf} at T_g (eq. 8). In the investigated system, melt
711 fragility varies smoothly with the SiO_2 and Al_2O_3 concentrations (Fig. 12a,b). Increasing melt
712 SiO_2 content leads to largely decrease melt fragility, an observation that agrees with previous
713 ones in alkali (e.g., Toplis et al., 1997a) and even alkaline-earth (e.g., Bechgaard et al., 2017)
714 aluminosilicate compositions. Changing the K/(K+Na) ratio does not lead to large changes in
715 fragility (Fig. 12c,d,e,f), in agreement with observations of Robert et al. (2019). At constant silica
716 concentration, depolymerized alkali silicate melts are slightly more fragile than polymerized
717 tectosilicate melts. i-Melt predicts that peraluminous Al-rich melts generally are more and more
718 fragile with increasing Al concentration. However, at ratios of Al/(Al+Na+K) higher than ~ 0.6 ,
719 the model extrapolates. This observation could indicate that (i) extrapolations are not fully
720 robust and should be considered with care, or (ii) high Al concentrations indeed lead to high
721 melt fragility.

722 The first question is important to consider, because as “intelligent” as they can be,
723 machine learning algorithms still are interpolative in nature. Therefore, it is not necessarily wise
724 to ask them to perform extrapolations. Here, we tested how the model generally behaves when

725 performing extrapolations beyond the chemical composition range that the training dataset
726 spans by (i) removing some density and optical refractive index data along the SiO_2 - Al_2O_3 join
727 and (ii) trying to predict a value for a composition very far from those included in its training
728 dataset, the T_g of Al_2O_3 . Regarding (i), the model tends to provide a constant value for density
729 or optical refractive index when asking to make predictions for compositions beyond those
730 included in its training set. This situation is both good and bad. It is good because it indicates
731 that the model does not “explode”, i.e. starts to predict small or large values very different
732 from the mean ones when extrapolating (this is what happens traditionally with polynomial
733 functions, for instance). It obviously is bad because it means that i-Melt will remain mostly
734 interpolative in nature for some parameters like fragility, at least for the moment. Turning to
735 the second test, we first estimated the Al_2O_3 T_g from the data of Secrist and MacKenzie (1965)
736 and Urbain et al. (1982). Secrist and MacKenzie (1965) estimated a viscosity of 4×10^{10} Pa·s at
737 1173 K from the rate of crystallization of vapor-formed Al_2O_3 amorphous films. Fitting the high
738 temperature viscosity data of Urbain et al. (1982) for Al_2O_3 and this point with equation 3, we
739 have for Al_2O_3 melt $A_{TVF} = -2.8 \pm 0.1$, $B_{TVF} = 1842 \pm 176$ and $C_{TVF} = 1035 \pm 19$, and $T_g = 1160 \pm 23$
740 K. i-Melt predicts a T_g of 963 K for Al_2O_3 . This T_g estimation is realistic (the model did not
741 ‘explode’) but significantly below the value calculated from viscosity data. This highlights that
742 extrapolations with models like i-Melt may produce apparently realistic results, but still may be
743 far from the true value.

744 With limited data, it is inevitable that i-Melt has to extrapolate for some predictions.
745 Following the above discussion, caution is needed. Fortunately, for some properties, results

746 appear to be broadly plausible. This is the case for $S^{conf}(T_g)$. For instance, the model predicts a
747 continuous decrease of $S^{conf}(T_g)$ with increasing Al₂O₃ in the peraluminous field (Fig. 11a,b), a
748 prediction that agrees with experimental data in sodium peraluminous melts (Le Losq et al.,
749 2014). To conclude, this discussion highlights that, if necessary, machine learning model
750 extrapolations can be performed but should be considered with care, making sure that
751 predictions are realistic compared to the known trends of material properties.

752

753 **4.5 Glass properties**

754 i-Melt predicts the viscous glass transition temperature well (Fig. 6a), and allows
755 systematic exploration of the variations of this parameter with melt composition (Fig. 13a,b). Its
756 variations are complex as it can be expected, because they depend on melt structure and are
757 also affected by chemical mixing effects (Fig. 10a). The model displays the well known decrease
758 of T_g with addition of alkali metals, and increase with addition of SiO₂, and, on a lesser extent,
759 Al₂O₃ (Fig. 13a,b). In the potassic aluminosilicate system, there is a local T_g maximum near the
760 KAlSi₂O₆ composition on the SiO₂-KAl₂O₄ binary, at ~ 66 mol% SiO₂ (Fig. 13b). This maximum
761 correlates with a maximum in liquidus temperatures ($T_{liquidus}$). That of leucite KAlSi₂O₆ is of 1693
762 °C (Schairer and Bowen, 1955). It corresponds to a local maximum along the SiO₂-KAl₂O₄ binary
763 that correlates with the T_g maximum observed in figure 13b. No such maximum in T_g is
764 observed on the sodic SiO₂-NaAl₂O₄ binary, in agreement with the absence of a $T_{liquidus}$
765 maximum along this binary (Schairer and Bowen, 1956). This agrees with the general

766 correlation between T_g and $T_{liquidus}$ (e.g., see Sakka and MacKenzie, 1971 and references
767 therein), leading us to suggest that a model such as i-Melt could also predict $T_{liquidus}$.

768 Compared to T_g , glass density or optical refractive index display simpler variations with
769 glass composition (Fig. 13c,d,e,f). As it is well known, glass density mostly depends on the
770 concentrations of Na_2O and Al_2O_3 added to SiO_2 . i-Melt reproduces this dependence well. The
771 glass optical refractive index variations show a different pattern, the addition of Al_2O_3 having a
772 greater effect than that of Na_2O at comparable molar contents. The optical refractive index
773 actually does not correlate strongly with any of the thermodynamic/dynamic variables. This is
774 expected because the optical refractive index is mostly controlled by the electronic properties
775 of the atoms present in the glass. Interestingly, the glass density correlates with fragility ($r_s =$
776 0.908). Similar variations are thus visible when comparing melt fragility and glass density in the
777 ternary sodium and potassium aluminosilicate diagrams (Figs. 12, 13).

778

779 **4.6 Volcanological implications**

780 Using i-Melt, we can address a variety of problems, including volcanological or
781 geochemical questions. As an example, we can look at why eruptions of silicic volcanoes may be
782 more explosive if the magma is rich in K and Al, an observation reported by Di Genova et al.
783 (2017). Indeed, those authors reported a correlation between the explosivity of silicic eruptions
784 and the contents of Al and K in the involved magmas. According to them, this correlation seems
785 to stand regardless of the other many critical parameters driving the dynamic of volcanic
786 eruptions, such as pre-eruptive volatile content, degassing path and nanolite content (e.g.,

787 Villemant and Boudon, 1998; Andújar and Scaillet, 2012; Di Genova et al., 2017, 2020; Moitra et
788 al., 2018; Cáceres et al., 2020). In figure 14, the compositions of silicic lavas, compiled by Di
789 Genova et al. (2017), are reported in term of agpaitic index ($= [\text{Fe}^{3+} + \text{Al}^{3+}] / [\text{Na}^+ + \text{K}^+ + \text{Ca}^{2+} +$
790 $\text{Mg}^{2+} + \text{Fe}^{2+}]$) and K/(K+Na) ratios. Two clusters of data points are visible. They are associated to
791 effusive and explosive eruptions. In their publication, Di Genova et al. (2017) show that this
792 clustering is primarily controlled by the agpaitic index and the K/(K+Na) ratio of the samples.
793 They observed that water and crystal contents of the melt also play an important role, but
794 those parameters alone cannot explain the observed correlation. The eruptive style of rhyolite
795 eruptions thus seems mainly influenced by small variations in magma composition, linked to
796 the influence of potassium and trivalent cations (Al³⁺ mainly, but also Fe³⁺) on the silicate melt
797 rheology.

798 Here, we can try to explore the thermodynamic origin of this correlation by using i-Melt.
799 Most of the lavas emitted at silicic volcanic systems, such as Yellowstone or Long Valley (U.S.A.),
800 contain more than 95 % of Na₂O, K₂O, Al₂O₃ and SiO₂. Therefore, melts in the Na₂O-K₂O-Al₂O₃-
801 SiO₂ system may be considered as simplified analogues of the lavas involved in silicic volcanic
802 eruptions, and i-Melt can be used to glimpse the links between eruptive dynamics and the
803 composition, structure, and properties of magmas. Of course, this will not take the effect of
804 volatile elements into account, but, as highlighted previously, the correlation reported by Di
805 Genova et al. (2017) is actually for dry compositions and, according to them, apparently
806 independent of melt water content. In any case, the following should be considered with care
807 and is here used primarily as an example of use of i-Melt. In the future, more complete versions

808 of models such as i-Melt will allow more robust exploration of the links between eruptive
809 dynamics and the composition, structure, and properties of magmas.

810 The two data point clusters observed in figure 14 are associated with different $S^{conf}(T_g)$
811 and R_{Raman} values. The data point cluster associated with explosive eruptions present $S^{conf}(T_g)$
812 values typically below $\sim 9 \text{ J mol}^{-1} \text{ K}^{-1}$ and R_{Raman} above ~ 1.5 ; the other cluster, associated to
813 effusive eruptions, present values in $S^{conf}(T_g)$ and R_{Raman} respectively above and below those
814 values. Decreasing the agpaitic index and increasing K/(K+Na) thus leads to an increase in
815 network polymerization and structuration, hence in fewer available configurations available for
816 viscous flow molecular movements. This results in increasing the melt viscosity, explaining
817 potentially the volcanic eruptive style chemical clustering observed in figure 14. It should be
818 emphasized that (i) the structural and associated entropic transition is actually smooth, and (ii)
819 the role of aluminium is more important than that of potassium: most of the variance in figure
820 14 is actually associated with variations in the agpaitic index. The first of those two
821 observations actually raise the question of a direct link between melt structure and the eruptive
822 dynamic. An indirect link could be seen in the way the Al/(Na+K) ratio affects the speciation and
823 valence of iron in aluminosilicate melts (Le Losq et al., 2020). Indeed, an increase in the
824 Al/(Na+K) ratio of aluminosilicate melts, in addition to strongly affecting melt polymerization
825 and properties (Figs. 12a,b, 13a,b), promotes iron reduction (Dickenson and Hess, 1982). Such a
826 phenomenon could promote the rapid appearance of iron-bearing nanolites, and hence act as
827 an accelerator in the increase of magma viscosity to promote the explosivity of the eruption
828 (Cáceres et al., 2020; Di Genova et al., 2020). This will be further promoted by the strong

829 influence of Al on the properties of melt involved in explosive eruptions. Indeed, the
830 explosive/effusive clusters visible in figure 14 mostly are separated by an agpaitic index of 1.
831 Below 1, most metal cations charge balance Al^{3+} and Fe^{3+} in tetrahedral coordination, and the
832 mobility of the melt at supercooled conditions is much lower than that of peralkaline melts
833 (e.g., Taylor and Rindone, 1970). Therefore, the correlation observed in figure 14 is not
834 surprising because rhyolite magmas can be peraluminous, with agpaitic index lower than 1.
835 Considering this, the fine chemical control observed in figure 14 will probably not hold for other
836 magma compositions, like andesites or phonolites, that have agpaitic index typically above 1.

837 In any case, those results showcase the potential of i-Melt. Extending this model to
838 embed the effects of Ca, Mg, Fe and water would provide the ability to explore and quantify
839 further the links between magma composition, structure, properties, and volcanic eruptive
840 styles.

841

842 **5. Conclusion**

843 The results presented here highlight that a deep learning framework like i-Melt can be
844 used for practical property predictions in the Earth and material sciences. The model has the
845 ability to predict many different glass and melt properties. It achieves good precision in the
846 glass forming domain. Extrapolations are possible but should be done with care. We see models
847 like i-Melt, therefore, as a pragmatic compromise between informative, accurate but limited
848 theoretical models and mono-task empirical models. i-Melt can readily be extended to include
849 quantities of interest across a range of domains and applications, including glass toughness and

850 hardness. The inclusion of properties that depend on a system including melt/glass plus other
851 components, like liquidus, seems more challenging at the moment. This could be due to an
852 intrinsic theoretical inconsistency as the model was trained to predict latent and observed
853 variables of a “melt/glass” object, not of a more complex system. However, this should be
854 tested further before any definitive conclusion. In any case, our results demonstrate that the
855 approach of combining machine learning with physical and thermodynamic models offers
856 exciting new perspectives.

857

858 **References and Notes.**

Adam G. and Gibbs J. H. (1965) *On the temperature dependence of cooperative relaxation properties in glass-forming liquids.* *J. Chem. Phys.* **43**, 139–146.

Allu A. R., Gaddam A., Ganisetti S., Balaji S., Siegel R., Mather G. C., Fabian M., Pascual M. J., Ditaranto N., Milius W., Senker J., Agarkov D. A., Kharton Vladislav. V. and Ferreira J. M. F. (2018) Structure and Crystallization of Alkaline-Earth Aluminosilicate Glasses: Prevention of the Alumina-Avoidance Principle. *J. Phys. Chem. B* **122**, 4737–4747.

Allwardt J. R., Poe B. T. and Stebbins J. F. (2005a) The effect of fictive temperature on Al coordination in high-pressure (10 GPa) sodium aluminosilicate glasses. *Am. Mineral.* **90**, 1453–1457.

Allwardt J. R., Stebbins J. F., Schmidt B. C., Frost D. J., Withers A. C. and Hirschmann M. M. (2005b) Aluminum coordination and the densification of high-pressure aluminosilicate glasses. *Am. Mineral.* **90**, 1218–1222.

Ando M. F., Benzine O., Pan Z., Garden J.-L., Wondraczek K., Grimm S., Schuster K. and Wondraczek L. (2018) Boson peak, heterogeneity and intermediate-range order in binary SiO₂-Al₂O₃ glasses. *Sci. Rep.* **8**. Available at: <http://www.nature.com/articles/s41598-018-23574-1> [Accessed April 4, 2018].

- Andújar J. and Scaillet B. (2012) Relationships between pre-eruptive conditions and eruptive styles of phonolite–trachyte magmas. *Lithos* **152**, 122–131.
- Avramov I. (2011) Dependence of the parameters of equations of viscous flow on chemical composition of silicate melts. *J. Non-Cryst. Solids* **357**, 3841–3846.
- Avramov I. and Milchev A. (1988) Effect of disorder on diffusion and viscosity in condensed systems. *J. Non-Cryst. Solids* **104**, 253–260.
- Bancroft G. M., Nesbitt H. W., Henderson G. S., O'Shaughnessy C., Withers A. C. and Neuville D. R. (2018) Lorentzian dominated lineshapes and linewidths for Raman symmetric stretch peaks (800–1200 cm⁻¹) in Qn ($n = 1–3$) species of alkali silicate glasses/melts. *J. Non-Cryst. Solids* **484**, 72–83.
- Bauchy M., Guillot B., Micoulaut M. and Sator N. (2013) Viscosity and viscosity anomalies of model silicates and magmas: A numerical investigation. *Chem. Geol.* **346**, 47–56.
- Bechgaard T. K., Mauro J. C., Bauchy M., Yue Y., Lamberson L. A., Jensen L. R. and Smedskjaer M. M. (2017) Fragility and configurational heat capacity of calcium aluminosilicate glass-forming liquids. *J. Non-Cryst. Solids* **461**, 24–34.
- Beckner W., M. Mao C. and Pfaendtner J. (2018) Statistical models are able to predict ionic liquid viscosity across a wide range of chemical functionalities and experimental conditions. *Mol. Syst. Des. Eng.* **3**, 253–263.
- Bell R. J., Bird N. F. and Dean P. (1968) The vibrational spectra of vitreous silica, germania and beryllium fluoride. *J. Phys. C Proc Phys Soc* **1**, 299–303.
- Bergstra J. and Bengio Y. (2012) Random search for hyper-parameter optimization. *J. Mach. Learn. Res.* **13**, 281–305.
- Bishop C. M. (2006) *Pattern recognition and machine learning*., Springer, New York.
- Bockris J. O., MacKenzie J. D. and Kitchener J. A. (1955) Viscous flow in silica and binary liquid silicates. *Trans. Faraday Soc.* **51**, 1734–1748.

Bottinga Y. and Richet P. (1996) Silicate melt structural relaxation: rheology, kinetics, and Adam-Gibbs theory. *Chem. Geol.* **128**, 129–141.

Bottinga Y., Richet P. and Sipp A. (1995) Viscosity regimes of homogeneous silicate melts. *Am. Mineral.* **80**, 305–318.

Bottinga Y. and Weill D. F. (1972) The viscosity of magmatic silicate liquids: a model for calculation. *Am. J. Sci.* **272**, 438–475.

Bowen N. L. (1928) *The evolution of igneous rocks.*, Oxford University Press.

Brawer S. A. and White W. B. (1975) Raman spectroscopic investigation of the structure of silicate glasses. I. The binary alkali silicates. *J. Chem. Phys.* **63**, 2421–2432.

Brawer S. A. and White W. B. (1977) Raman spectroscopic investigation of the structure of silicate glasses (II). Soda-alkaline earth-alumina ternary and quaternary glasses. *J. Non-Cryst. Solids* **23**, 261–278.

Breiman L. and Breiman L. (1996) Bagging Predictors. In *Machine Learning* pp. 123–140.

Cáceres F., Wadsworth F. B., Scheu B., Colombier M., Madonna C., Cimarelli C., Hess K.-U., Kaliwoda M., Ruthensteiner B. and Dingwell D. B. (2020) Can nanolites enhance eruption explosivity? *Geology* **48**, 997–1001.

Caruana R. (1997) Multitask Learning. *Mach. Learn.* **28**, 41–75.

Cassar D. R. (2020) ViscNet: neural network for predicting the fragility index and the temperature-dependency of viscosity. *ArXiv200703719 Cond-Mat Physicsphysics*. Available at: <http://arxiv.org/abs/2007.03719> [Accessed January 14, 2021].

Cassidy M., Manga M., Cashman K. and Bachmann O. (2018) Controls on explosive-effusive volcanic eruption styles. *Nat. Commun.* **9**, 2839.

Cohen M. H. and Grest G. S. (1979) Liquid-glass transition, a free-volume approach. *Phys. Rev. B* **20**, 1077.

Cohen M. H. and Grest G. S. (1984) The nature of the glass transition. *J. Non-Cryst. Solids* **61–62**, 749–759.

Day D. E. (1976) Mixed alkali glasses - Their properties and uses. *J. Non-Cryst. Solids* **21**, 343–372.

Di Genova D., Brooker R. A., Mader H. M., Drewitt J. W. E., Longo A., Deubener J., Neuville D. R., Fanara S., Shebanova O., Anzellini S., Arzilli F., Bamber E. C., Hennet L., La Spina G. and Miyajima N. (2020) In situ observation of nanolite growth in volcanic melt: A driving force for explosive eruptions. *Sci. Adv.* **6**, eabb0413.

Di Genova D., Kolzenburg S., Wiesmaier S., Dallanave E., Neuville D. R., Hess K. U. and Dingwell D. B. (2017) A compositional tipping point governing the mobilization and eruption style of rhyolitic magma. *Nature* **552**, 235.

Dickenson M. P. and Hess P. C. (1982) Redox equilibria and the structural role of iron in alumino-silicate melts. *Contrib. Mineral. Petrol.* **78**, 352–357.

Dingwell D. B. (1996) Volcanic Dilemma - Flow or Blow? *Science* **273**, 1054–1055.

Drewitt J. W. E., Jahn S., Sanloup C., de Grouchy C., Garbarino G. and Hennet L. (2015) Development of chemical and topological structure in aluminosilicate liquids and glasses at high pressure. *J Phys Condens Matter*, 105103.

Duan X. (2014) A model for calculating the viscosity of natural iron-bearing silicate melts over a wide range of temperatures, pressures, oxygen fugacites, and compositions. *Am. Mineral.* **99**, 2378–2388.

Dufils T., Folliet N., Mantisi B., Sator N. and Guillot B. (2017) Properties of magmatic liquids by molecular dynamics simulation: The example of a MORB melt. *Chem. Geol.* **461**, 34–46.

Furukawa T., Fox K. E. and White W. B. (1981) Raman spectroscopic investigation of the structure of silicate glasses. III. Raman intensities and structural units in sodium silicate glasses. *J. Chem. Phys.* **75**, 3226–3237.

Giordano D. and Russell J. K. (2017) The heat capacity of hydrous multicomponent natural melts and glasses. *Chemical Geology*. Available at: <http://www.sciencedirect.com/science/article/pii/S000925411630451X> [Accessed December 15, 2016].

Giordano D. and Russell J. K. (2018) Towards a structural model for the viscosity of geological melts. *Earth Planet. Sci. Lett.* **501**, 202–212.

Giordano D., Russell J. K. and Dingwell D. B. (2008) Viscosity of magmatic liquids: A model. *Earth Planet. Sci. Lett.* **271**, 123–134.

Glorot X., Bordes A. and Bengio Y. (2011) Deep sparse rectifier neural networks. In *International Conference on Artificial Intelligence and Statistics* pp. 315–323. Available at:
http://machinelearning.wustl.edu/mlpapers/paper_files/AISTATS2011_GlorotBB11.pdf [Accessed June 15, 2016].

Goldstein M. (2011) On the reality of the residual entropy of glasses and disordered crystals: The entropy of mixing. *J. Non-Cryst. Solids* **357**, 463–465.

Gonnermann H. M. (2015) Magma Fragmentation. *Annu. Rev. Earth Planet. Sci.* **43**, 431–458.

Gonnermann H. M. and Manga M. (2013) Dynamics of magma ascent in the volcanic conduit. In *Modeling Volcanic Processes: The Physics and Mathematics of Volcanism* (eds. S. A. Fagents, T. K. P. Gregg, and R. M. C. Lopes).

Cambridge University Press. pp. 55–84. Available at:
https://www.cambridge.org/core/product/identifier/CBO9781139021562A011/type/book_part [Accessed December 13, 2018].

Goodfellow I., Bengio Y. and Courville A. (2016) *Deep Learning.*, MIT Press. Available at:
<http://www.deeplearningbook.org>.

Guillot B. and Sator N. (2007) A computer simulation study of natural silicate melts. Part I: Low pressure properties. *Geochim. Cosmochim. Acta* **71**, 1249–1265.

Hess K. U. and Dingwell D. D. (1996) Viscosities of hydrous leucogranitic melts: A non-Arrhenian model. *Am. Mineral.* **81**, 1297–1300.

Hodge I. M. (1994) Enthalpy relaxation and recovery in amorphous materials. *J. Non-Cryst. Solids* **169**, 211–266.

Hui H. and Zhang Y. (2007) Toward a general viscosity equation for natural anhydrous and hydrous silicate melts. *Geochim. Cosmochim. Acta* **71**, 403–416.

Hummel W. and Arndt J. (1985) Variation of viscosity with temperature and composition in the plagioclase system. *Contrib. Mineral. Petrol.* **90**, 83–92.

Isard J. O. (1969) The mixed alkali effect in glass. *J. Non-Cryst. Solids* **1**, 235–261.

Iuga D., Morais C., Gan Z., Neuville D. R., Cormier L. and Massiot D. (2005) NMR Heteronuclear Correlation between Quadrupolar Nuclei in Solids. *J. Am. Chem. Soc.* **127**, 11540–11541.

Jackson W. E., Brown G. E. and Ponader C. W. (1987) X-ray absorption study of the potassium coordination environment in glasses from the NaAlSi₃O₈-KAlSi₃O₈ binary. *J. Non-Cryst. Solids* **93**, 311–322.

Jarry P. and Richet P. (2001) Unmixing in sodium-silicate melts: influence on viscosity and heat capacity. *J. Non-Cryst. Solids* **293–295**, 232–237.

Karpatne A., Watkins W., Read J. and Kumar V. (2018) Physics-guided Neural Networks (PGNN): An Application in Lake Temperature Modeling. *ArXiv171011431 Phys. Stat.* Available at: <http://arxiv.org/abs/1710.11431> [Accessed January 14, 2021].

Kiczenski T. J., Du L.-S. and Stebbins J. (2005) The effect of fictive temperature on the structure of E-glass: A high resolution, multinuclear NMR study. *J. Non-Cryst. Solids* **351**, 3571–3578.

Koroleva O. N., Anfilogov V. N., Shatskiy A. and Litasov K. D. (2013) Structure of Na₂O–SiO₂ melt as a function of composition: In situ Raman spectroscopic study. *J. Non-Cryst. Solids* **375**, 62–68.

Le Losq C., Berry A. J., Kendrick M. A., Neuville D. R. and O'Neill H. St. C. (2019a) Determination of the oxidation state of iron in Mid-Ocean Ridge basalt glasses by Raman spectroscopy. *Am. Mineral.* **104**, 1032–1042.

Le Losq C., Cicconi M. R., Greaves G. N. and Neuville D. R. (2019b) Silicate Glasses. In *Handbook of Glass* Springer. Available at: <https://www.springer.com/us/book/9783319937267>.

Le Losq C., Cicconi M. R. and Neuville D. (2020) Iron in silicate glasses and melts: implications for volcanological processes. *Earth Space Sci. Open Arch.* Available at: <http://www.essoar.org/doi/10.1002/essoar.10503261.1> [Accessed June 8, 2020].

Le Losq C. and Neuville D. R. (2013) Effect of the Na/K mixing on the structure and the rheology of tectosilicate silica-rich melts. *Chem. Geol.* **346**, 57–71.

Le Losq C. and Neuville D. R. (2017) Molecular structure, configurational entropy and viscosity of silicate melts: Link through the Adam and Gibbs theory of viscous flow. *J. Non-Cryst. Solids* **463**, 175–188.

Le Losq C., Neuville D. R., Chen W., Florian P., Massiot D., Zhou Z. and Greaves G. N. (2017) Percolation channels: a universal idea to describe the atomic structure and dynamics of glasses and melts. *Sci. Rep.* **7**, 16490.

Le Losq C., Neuville D. R., Florian P., Henderson G. S. and Massiot D. (2014) The role of Al³⁺ on rheology and structural changes of sodium silicate and aluminosilicate glasses and melts. *Geochim. Cosmochim. Acta* **126**, 495–517.

Lee S. K. (2005) Structure and the extent of disorder in quaternary (Ca-Mg and Ca-Na) aluminosilicate glasses and melts. *Am. Mineral.* **90**, 1393–1401.

Lee S. K., Kim H.-I., Kim E. J., Mun K. Y. and Ryu S. (2016) Extent of Disorder in Magnesium Aluminosilicate Glasses: Insights from ²⁷Al and ¹⁷O NMR. *J. Phys. Chem. C* **120**, 737–749.

Lee S. K., Mysen B. O. and Cody G. D. (2003) Chemical order in mixed-cation silicate glasses and melts. *Phys. Rev. B* **68**, 214206.

Lee S. K. and Stebbins J. F. (1999) The degree of aluminum avoidance in aluminosilicate glasses. *Am. Mineral.* **84**, 937–945.

Liu G., Zhao D. and Zuo Y. (2015) Modified Adam–Gibbs models based on free volume concept and their application in the enthalpy relaxation of glassy polystyrene. *J. Non-Cryst. Solids* **417–418**, 52–59.

Maehara T., Yano T. and Shibata S. (2005) Structural rules of phase separation in alkali silicate melts analyzed by high-temperature Raman spectroscopy. , 8.

Maekawa H., Maekawa T., Kawamura K. and Yokokawa T. (1991) The structural groups of alkali silicate glasses determined from ²⁹Si MAS-NMR. *J. Non-Cryst. Solids* **127**, 53–64.

Malfait W. J. (2009) Quantitative Raman spectroscopy: speciation of cesium silicate glasses. *J. Raman Spectrosc.* **40**, 1895–1901.

- Malfait W. J., Zakaznova-Herzog V. P. and Halter W. E. (2007) Quantitative Raman spectroscopy: high-temperature speciation of potassium silicate melts. *J. Non-Cryst. Solids* **353**, 4029–4042.
- Massiot D., Fayon F., Montouillout V., Pellerin N., Hiet J., Roiland C., Florian P., Coutures J., Cormier L. and Neuville D. (2008) Structure and dynamics of oxide melts and glasses: A view from multinuclear and high temperature NMR. *J. Non-Cryst. Solids* **354**, 249–254.
- Matson D. W. and Sharma S. K. (1985) Structures of sodium alumino- and gallosilicate glasses and their germanium analogs. *Geochim. Cosmochim. Acta* **49**, 1913–1924.
- Mauro J. C., Yue Y., Ellison A. J., Gupta P. K. and Allan D. C. (2009) Viscosity of glass-forming liquids. *Proc. Natl. Acad. Sci.* **106**, 19780–19784.
- Mazurin O. V., Streltsina M. V., and Shvaiko-Shvaikovskaya (1987) *Handbook of glass data.*, Elsevier.
- McKeown D. A., Waychunas G. A. and Brown G. E. (1985) Exafs and xanes study of the local coordination environment of sodium in a series of silica-rich glasses and selected minerals within the Na₂O-Al₂O₃-SiO₂ system. *J. Non-Cryst. Solids* **74**, 325–348.
- McMillan P. F. (1984) Structural studies of silicate glasses and melts - Applications and limitations of Raman spectroscopy. *Am. Mineral.* **69**, 622–644.
- Merzbacher C. I. and White W. B. (1991) The structure of alkaline earth aluminosilicate glasses as determined by vibrational spectroscopy. *J. Non-Cryst. Solids* **130**, 18–34.
- Moitra P., Gonnermann H. M., Houghton B. F. and Tiwary C. S. (2018) Fragmentation and Plinian eruption of crystallizing basaltic magma. *Earth Planet. Sci. Lett.* **500**, 97–104.
- Morin E. I., Wu J. and Stebbins J. F. (2014) Modifier cation (Ba, Ca, La, Y) field strength effects on aluminum and boron coordination in aluminoborosilicate glasses: the roles of fictive temperature and boron content. *Appl. Phys. A* **116**, 479–490.
- Murphy K. P. (2012) *Machine Learning: A Probabilistic Perspective.*, The MIT Press, Cambridge, Massachusetts.

Mysen B. O. (1995) Experimental, in situ, high-temperature studies of properties and structure of silicate melts relevant to magmatic processes. *Eur. J. Mineral.* **7**, 745–766.

Mysen B. O. (1996) Haploandesitic melts at magmatic temperatures: In situ, high-temperature structure and properties of melts along the join K^{147°C} at atmospheric pressure. *Geochim. Cosmochim. Acta* **60**, 3665–3685.

Mysen B. O. (1991) Relations Between Structure, Redox Equilibria of Iron, and Properties of Magmatic Liquids. In *Physical Chemistry of Magmas Advances in Physical Geochemistry*. Springer, New York, NY. pp. 41–98. Available at: https://link.springer.com/chapter/10.1007/978-1-4612-3128-8_2 [Accessed June 22, 2018].

Mysen B. O. (1990) Role of Al in depolymerized, peralkaline aluminosilicate melts in the systems Li₂O-Al₂O₃-SiO₂, Na₂O-Al₂O₃-SiO₂, and K₂O-Al₂O₃-SiO₂. *Am. Mineral.* **75**, 120–134.

Mysen B. O. (1999) Structure and properties of magmatic liquids: From haplobasalt to haploandesite. *Geochim. Cosmochim. Acta* **63**, 95–112.

Mysen B. O. (1988) *Structure and properties of silicate melts*. ed. W. S. FYFE, Elsevier, Amsterdam-Oxford-New York-Tokyo.

Mysen B. O. (2007) The solution behavior of H₂O in peralkaline aluminosilicate melts at high pressure with implications for properties of hydrous melts. *Geochim. Cosmochim. Acta* **71**, 1820–1834.

Mysen B. O., Finger L. W., Virgo D. and Seifert F. A. (1982) Curve-fitting of Raman spectra of silicate glasses. *Am. Mineral.* **67**, 686–695.

Mysen B. O. and Frantz J. D. (1992) Raman spectroscopy of silicate melts at magmatic temperatures: Na₂O-SiO₂, K₂O-SiO₂ and Li₂O-SiO₂ binary compositions in the temperature range 25–1475°C. *Chem. Geol.* **96**, 321–332.

Mysen B. O., Lucier A. and Cody G. D. (2003) The structural behavior of Al³⁺ in peralkaline melts and glasses in the system Na₂O-Al₂O₃-SiO₂. *Am. Mineral.* **88**, 1668–1678.

Mysen B. O. and Richet P. (2019) *Silicate Glasses and Melts*. 2nd ed., Elsevier.

Mysen B. O. and Toplis M. J. (2007) Structural behavior of Al³⁺ in peralkaline, metaluminous, and peraluminous silicate melts and glasses at ambient pressure. *Am. Mineral.* **92**, 933–946.

Mysen B. O., Virgo D. and Scarfe C. M. (1980) Relations between the anionic structure and viscosity of silicate melts - A Raman spectroscopic study. *Am. Mineral.* **65**, 690–710.

Mysen B. O., Virgo D. and Seifert F. A. (1982) The structure of silicate melts: Implications for chemical and physical properties of natural magma. *Rev. Geophys.* **20**, 353–383.

Nesbitt H. W., Henderson G. S., Bancroft G. M. and Neuville D. R. (2021) Spectral Resolution and Raman Q3 and Q2 cross sections in ~40 mol% Na₂O glasses. *Chem. Geol.* **562**, 120040.

Nesbitt H. W., O'Shaughnessy C., Henderson G. S., Michael Bancroft G. and Neuville D. R. (2019) Factors affecting line shapes and intensities of Q3 and Q4 Raman bands of Cs silicate glasses. *Chem. Geol.* **505**, 1–11.

Neuville D., Cormier L., Montouillout V. and Massiot D. (2007) Local Al site distribution in aluminosilicate glasses by ²⁷Al MQMAS NMR. *J. Non-Cryst. Solids* **353**, 180–184.

Neuville D. R. (2006) Viscosity, structure and mixing in (Ca, Na) silicate melts. *Chem. Geol.* **229**, 28–41.

Neuville D. R., Cormier L., de Ligny D., Roux J., Flank A.-M. and Lagarde P. (2008) Environments around Al, Si, and Ca in aluminate and aluminosilicate melts by X-ray absorption spectroscopy at high temperature. *Am. Mineral.* **93**, 228–234.

Neuville D. R., Cormier L., Montouillout V., Florian P., Millot F., Rifflet J.-C. and Massiot D. (2008) Structure of Mg- and Mg/Ca aluminosilicate glasses: ²⁷Al NMR and Raman spectroscopy investigations. *Am. Mineral.* **93**, 1721–1731.

Neuville D. R. and Mysen B. O. (1996) Role of aluminium in the silicate network: In situ, high-temperature study of glasses and melts on the join SiO₂-NaAlO₂. *Geochim. Cosmochim. Acta* **60**, 1727–1737.

Neuville D. R. and Richet P. (1991) Viscosity and mixing in molten (Ca, Mg) pyroxenes and garnets. *Geochim. Cosmochim. Acta* **55**, 1011–1019.

Oglesby J. V., Zhao P. and Stebbins J. F. (2002) Oxygen sites in hydrous aluminosilicate glasses: The role of Al-O-Al and H₂O. *Geochim. Cosmochim. Acta* **66**, 291–301.

Okuno M., Zotov N., Schmücker M. and Schneider H. (2005) Structure of SiO₂–Al₂O₃ glasses: Combined X-ray diffraction, IR and Raman studies. *J. Non-Cryst. Solids* **351**, 1032–1038.

Paduszyński K. and Domańska U. (2014) Viscosity of Ionic Liquids: An Extensive Database and a New Group Contribution Model Based on a Feed-Forward Artificial Neural Network. *J. Chem. Inf. Model.* **54**, 1311–1324.

Papale P. (1999) Strain-induced magma fragmentation in explosive eruptions. *Nature* **397**, 425–428.

Paszke A., Gross S., Massa F., Lerer A., Bradbury J., Chanan G., Killeen T., Lin Z., Gimelshein N., Antiga L., Desmaison A., Kopf A., Yang E., DeVito Z., Raison M., Tejani A., Chilamkurthy S., Steiner B., Fang L., Bai J. and Chintala S. (2019) PyTorch: An Imperative Style, High-Performance Deep Learning Library. *Adv. Neural Inf. Process. Syst.* **32**, 8026–8037.

Persikov E. S. (1991) The viscosity of magmatic liquids : experiment, generalized patterns. A model for calculation and prediction. *Applications. Adv. Phys. Geochem.* **9**, 1–40.

Rammensee W. and Fraser D. G. (1982) Determination of activities in silicate melts by Knudsen cell mass spectrometry - I. The system NaAlSi₃O₈-KAlSi₃O₈. *Geochim. Cosmochim. Acta* **46**, 2269–2278.

Rapaport D. C. (2004) *The art of molecular dynamics simulation*. 2nd ed., Cambridge University Press, Cambridge, U.K.

Ren Y., Xu X., Yang S., Nie L. and Chen Y. (2020) A Physics-Based Neural-Network Way to Perform Seismic Full Waveform Inversion. *IEEE Access* **8**, 112266–112277.

Richet P. (1987) Heat capacity of silicate glasses. *Chem. Geol.* **62**, 111–124.

Richet P. (1984) Viscosity and configurational entropy of silicate melts. *Geochim. Cosmochim. Acta* **48**, 471–483.

Richet P. and Bottinga Y. (1984) Glass transitions and thermodynamic properties of amorphous SiO₂, NaAlSi_nO_{2n+2} and KAlSi₃O₈. *Geochim. Cosmochim. Acta* **48**, 453–470.

Richet P. and Bottinga Y. (1985) Heat capacity of aluminum-free liquid silicates. *Geochim. Cosmochim. Acta* **49**, 471–486.

Riebling E. F. (1966) Structure of sodium aluminosilicate melts containing at least 50 mol% SiO₂ at 1500°C. *J. Chem. Phys.* **44**, 2857–2865.

Robert G., Smith R. A. and Whittington A. G. (2019) Viscosity of melts in the NaAlSiO₄-KAlSiO₄-SiO₂ system: Configurational entropy modelling. *J. Non-Cryst. Solids* **524**, 119635.

Robert G., Whittington A. G., Stechern A. and Behrens H. (2013) The effect of water on the viscosity of a synthetic calc-alkaline basaltic andesite. *Chem. Geol.* **346**, 135–148.

Russell J. K. and Giordano D. (2017) Modelling configurational entropy of silicate melts. *Chem. Geol.* **461**, 140–151.

Russell J. K., Giordano D. and Dingwell D. B. (2003) High-temperature limits on viscosity of non-Arrhenian silicate melts. *Am. Mineral.* **88**, 1390–1394.

Sakka S. and MacKenzie J. D. (1971) Relation between apparent glass transition temperature and liquids temperature for inorganic glasses. *J. Non-Cryst. Solids* **6**, 145–162.

Schairer J. F. and Bowen N. L. (1955) The system K₂O-Al₂O₃-SiO₂. *Am. J. Sci.* **253**, 681–746.

Schairer J. F. and Bowen N. L. (1956) The system Na₂O-Al₂O₃-SiO₂. *Am. J. Sci.* **254**, 129–195.

Scherer G. W. (1984) Use of the Adam-Gibbs Equation in the Analysis of Structural Relaxation. *J. Am. Ceram. Soc.* **67**, 504–511.

Sechrist D. R., MacKenzie J. D., Lee E. H. and Rogers T. G. (1965) Identification of Uncommon Noncrystalline Solids as Glasses. *J. Am. Ceram. Soc.* **48**, 487–491.

Sehlke A. and Whittington A. G. (2016) The viscosity of planetary tholeiitic melts: A configurational entropy model. *Geochim. Cosmochim. Acta* **191**, 277–299.

Seifert F., Mysen B. O. and Virgo D. (1982) Three-dimensional network structure of quenched melts (glass) in the systems SiO₂-NaAlO₂, SiO₂-CaAl₂O₄ and SiO₂-MgAl₂O₄. *Am. Mineral.* **67**, 696–717.

Sen P. N. and Thorpe M. F. (1977) Phonons in AX_2 glasses: From molecular to band-like modes. *Phys. Rev. B* **15**, 4030–4038.

Shaw H. R. (1972) Viscosities of magmatic silicate liquids: an empirical method of prediction. *Am. J. Sci.* **272**, 870–893.

Srivastava N., Hinton G., Krizhevsky A., Sutskever I. and Salakhutdinov R. (2014) Dropout: A Simple Way to Prevent Neural Networks from Overfitting. *J. Mach. Learn. Res.* **15**, 1929–1958.

Starodub K., Wu G., Yazhenskikh E., Müller M., Khvan A. and Kondratiev A. (2019) An Avramov-based viscosity model for the $\text{SiO}_2\text{-Al}_2\text{O}_3\text{-Na}_2\text{O}\text{-K}_2\text{O}$ system in a wide temperature range. *Ceram. Int.* **45**, 12169–12181.

Stebbins J. F., Carmichael I. S. E. and Moret L. K. (1984) Heat capacities and entropies of silicate liquids and glasses. *Contrib. Mineral. Petrol.* **86**, 131–148.

Stebbins J. F., Dubinsky E. V., Kanehashi K. and Kelsey K. E. (2008) Temperature effects on non-bridging oxygen and aluminum coordination number in calcium aluminosilicate glasses and melts. *Geochim. Cosmochim. Acta* **72**, 910–925.

Stebbins J. F., Kroeker S., Lee S. K. and Kiczenski T. J. (2000) Quantification of five- and six-coordinated aluminum ions in aluminosilicate and fluoride-containing glasses by high-field, high-resolution ^{27}Al NMR. *J. Non-Cryst. Solids* **275**, 1–6.

Stebbins J. F., Lee S. K. and Oglesby J. V. (1999) Al-O-Al oxygen sites in crystalline aluminates and aluminosilicate glasses; high-resolution oxygen-17 NMR results. *Am. Mineral.* **84**, 983–986.

Stebbins J. F. and Xu Z. (1997) NMR evidence for excess non-bridging oxygen in an aluminosilicate glass. *Nature* **390**, 60–62.

Tangeman J. A. and Lange R. A. (1998) The effect of Al^{3+} , Fe^{3+} , and Ti^{4+} on the configurational heat capacities of sodium silicate liquids. *Physic Chem. Miner.* **26**, 83–99.

Taylor T. D. and Rindone G. E. (1970) Properties of Soda Aluminosilicate Glasses: V, Low-Temperature Viscosities. *J. Am. Ceram. Soc.* **53**, 692–695.

Thompson L. M. and Stebbins J. F. (2013) Interaction between composition and temperature effects on non-bridging oxygen and high-coordinated aluminum in calcium aluminosilicate glasses. *Am. Mineral.* **98**, 1980–1987.

Thompson L. M. and Stebbins J. F. (2011) Non-bridging oxygen and high-coordinated aluminum in metaluminous and peraluminous calcium and potassium aluminosilicate glasses: High-resolution ^{17}O and ^{27}Al MAS NMR results. *Am. Mineral.* **96**, 841–853.

Thompson L. M. and Stebbins J. F. (2012) Non-stoichiometric non-bridging oxygens and five-coordinated aluminum in alkaline earth aluminosilicate glasses: Effect of modifier cation size. *J. Non-Cryst. Solids* **358**, 1783–1789.

Toplis M. J. (1998) Energy barriers to viscous flow and the prediction of glass transition temperatures of molten silicates. *Am. Mineral.* **83**, 480–490.

Toplis M. J. (2001) Quantitative links between microscopic properties and viscosity of liquids in the system SiO_2 – Na_2O . *Chem. Geol.* **174**, 321–331.

Toplis M. J., Dingwell D. B., Hess K.-U. and Lenci T. (1997a) Viscosity, fragility, and configurational entropy of melts along the join SiO_2 – NaAlSiO_4 . *Am. Mineral.* **82**, 979–990.

Toplis M. J., Dingwell D. B. and Lenci T. (1997b) Peraluminous viscosity maxima in Na_2O – Al_2O_3 – SiO_2 liquids: The role of triclusters in tectosilicate melts. *Geochim. Cosmochim. Acta* **61**, 2605–2612.

Toplis M. J., Kohn S. C., Smith M. E. and Poplett J. F. (2000) Fivefold-coordinated aluminum in tectosilicate glasses observed by triple quantum MAS NMR. *Am. Mineral.* **85**, 1556–1560.

Urbain G., Bottinga Y. and Richet P. (1982) Viscosity of liquid silica, silicates and alumino-silicates. *Geochim. Cosmochim. Acta* **46**, 1061–1072.

Varshneya A. K. and Bihuniak P. P. (2017) Cover screens for personal electronic devices: Strengthened glass or sapphire? *Am. Ceram. Soc. Bull.* **96**, 6.

Villemant B. and Boudon G. (1998) Transition from dome-forming to plinian eruptive styles controlled by H₂O and Cl degassing. *Nature* **392**, 65–69.

Virgo D., Mysen B. O. and Kushiro I. (1980) Anionic constitution of 1-Atmosphere silicate melts: implications for the structure of igneous melts. *Science* **208**, 1371–1373.

Vuilleumier R., Sator N. and Guillot B. (2009) Computer modeling of natural silicate melts: What can we learn from ab initio simulations. *Geochim. Cosmochim. Acta* **73**, 6313–6339.

Wang Y., Sakamaki T., Skinner L. B., Jing Z., Yu T., Kono Y., Park C., Shen G., Rivers M. L. and Sutton S. R. (2014) Atomistic insight into viscosity and density of silicate melts under pressure. *Nat. Commun.* **5**, 3241.

Webb S. L. L. (2008) Configurational heat capacity of Na₂O–CaO–Al₂O₃–SiO₂ melts. *Chem. Geol.* **256**, 92–101.

Willard J., Jia X., Xu S., Steinbach M. and Kumar V. (2020) Integrating Physics-Based Modeling with Machine Learning: A Survey. *ArXiv200304919 Phys. Stat.* Available at: <http://arxiv.org/abs/2003.04919> [Accessed January 14, 2021].

Xiang Y., Du J., Smedskjaer M. M. and Mauro J. C. (2013) Structure and properties of sodium aluminosilicate glasses from molecular dynamics simulations. *J. Chem. Phys.* **139**, 044507.

You J.-L., Jiang G.-C., Hou H.-Y., Chen H., Wu Y.-Q. and Xu K.-D. (2005) Quantum chemistry study on superstructure and Raman spectra of binary sodium silicates. *J. Raman Spectrosc.* **36**, 237–249.

Zakaznova-Herzog V. P., Malfait W. J., Herzog F. and Halter W. E. (2007) Quantitative Raman spectroscopy: Principles and application to potassium silicate glasses. *J. Non-Cryst. Solids* **353**, 4015–4028.

859

860 **Acknowledgments:** CLL thanks Malcolm Sambridge (Seismology & Mathematical Geophysics,
861 RSES, Australian National University), Lexing Xie and Cheng Soon Ong (CECS, Australian National
862 University), for various discussions and their advice regarding optimization and machine
863 learning.

864

865 **Funding:** CLL acknowledges funding from a Chaire d'Excellence IDEX19C627X/FD070/D110
866 from the IdEX Université de Paris ANR-18-IDEX-0001, from the Australian Research Council
867 Laureate Fellowship FL1600000 to Prof. Hugh O'Neill (ANU-RSES) as well as from the
868 Postdoctoral Fellowship of the Carnegie Institution for Science during the realization of this
869 project. APV acknowledges support from the ARC via grants DE180100040 and DP200100053.

870

871 **Author contributions:** CLL designed the study, collected the data, performed Raman and
872 viscosity experiments, and developed the deep learning framework and the associated
873 computer code. AV and BOM helped in the design of the neural network. CLL, BOM and DN
874 performed Raman measurements. CLL and AV drafted the manuscript. All authors contributed
875 to the final version of the manuscript.

876

877 **Competing interests:** Authors declare no competing interests.

878

879 **Materials & Correspondence:** All the data are available in the main text or the supplementary
880 materials. The computer code to reproduce the results of this study is available as a Python
881 library at the web address <https://github.com/charlesll/neuravi> (open access will be provided
882 upon acceptance). Correspondence can be addressed to the corresponding author.

883

Glass name		%SiO ₂	%Al ₂ O ₃	%K ₂ O	%Na ₂ O	Density, g cm ⁻¹
KA80.05	nom. mol%	80.00	5.00	15.00	0.00	
	nom. wt%	71.40	7.60	21.00	0.00	
	an. wt%	74.8(4)	7.6(1)	15.1(2)	0.00(4)	2.320(1)
KA72.07	nom. mol%	72.00	7.00	21.00	0.00	
	nom. wt%	61.60	10.20	28.20	0.00	
	an. wt%	61.4(3)	10.2(2)	27.4(3)	0.00(2)	2.408(1)
KA65.09	nom. mol%	65.00	8.75	26.25	0.00	
	nom. wt%	53.70	12.30	34.00	0.00	
	an. wt%	53.3(5)	12.5(4)	31.7(3)	0.00(3)	2.451(9)
NA65.09	nom. mol%	65.00	8.75	0.00	26.25	
	nom. wt%	60.79	13.89	0.00	25.32	
	an. wt%	61.7(4)	13.7(2)	0.03(2)	24.5(7)	2.472(4)
NA58.10	nom. mol%	58.00	10.50	0.00	31.50	
	nom. wt%	53.55	16.45	0.00	30.00	
	an. wt%	54.6(3)	16.4(2)	0.05(2)	28.9(4)	2.502(5)

887 **Table 1.** Composition of the synthesized glasses. Nominal (nom.) and analyzed (an.)
 888 compositions are reported. Standard deviations on measured values on 10 different spots (for

889 EPMA measurements) or glass chips (for density measurements) are given in parenthesis (1σ
890 confidence interval).

891

892

893

T, K	KA80.05	T, K	KA72.07	T, K	KA65.09	T, K	NA65.09	T, K	NA58.10
1013.1	9.10	921.5	9.37	941.3	9.55	834.0	9.01	827.3	10.10
1001.8	9.32	891.0	10.17	935.1	9.71	829.0	9.18	836.9	9.73
989.6	9.51	872.0	10.75	919.4	10.13	813.8	9.61	817.6	10.51
981.6	9.78	852.0	11.40	913.6	10.32	803.2	9.94	796.2	11.42
967.6	10.05			898.7	10.78	798.6	10.09	805.7	10.97
949.7	10.50			892.0	10.96	787.5	10.50	847.1	9.36
940.3	10.83			882.1	11.28	779.9	10.81	855.9	9.09
928.2	11.05			867.3	11.86	773.7	11.07	828.3	10.01
918.4	11.32			855.4	12.29	772.9	11.07	834.4	9.81
905.1	11.63					762.6	11.52	787.4	11.80
896.6	11.92					756.3	11.74	777.4	12.36
						752.1	11.95		

894

895 **Table 2.** Viscosity measurements in \log_{10} Pa·s. Errors on viscosity are lower or equal to 0.03896 \log_{10} Pa·s.

897

898

Data subset:	Training	Validation	Testing
Adam-Gibbs (eq. 1, log Pa·s)	0.34	0.22	0.35
Free Volume (eq. 2, log Pa·s)	0.49	0.24	0.35
TVF (eq. 3, log Pa·s)	0.40	0.25	0.38
MYEGA (eq. 5, log Pa·s)	0.38	0.26	0.36
Avramov-Milchev (eq. 4, log Pa·s)	0.35	0.24	0.35
Density (g cm⁻¹)	0.04	0.05	0.05
Raman spectra (%, LAD)	18	14	-
Refractive index	0.003	0.003	0.005

899

900 **Table 3: Root-mean-square errors (RMSE) of the deep learning framework.** RMSE
 901 calculated between measured and predicted melt viscosity, density, refractive index, except for
 902 Raman spectra where a different metric is used (median least absolute deviation LAD).

903

904

905 **Figure 1.** Melt viscosity (**a**), glass Raman spectroscopy (**b**), glass density (**C**) and glass refractive
906 index (**d**) datasets used in this publication. Each symbol corresponds to a sample. The glass-
907 forming domain at usual laboratory cooling rates is indicated in grey.

908 **Figure 2.** Schematic of i-Melt. An artificial neural network takes input melt composition, and
909 outputs various melt and glass properties. Once trained, relationships between chemistry,
910 structure and properties of melts and glasses can be systematically explored.

911 **Figure 3.** Neural network architecture and dropout influence on predictive performance.
912 Predictive performance was documented using the RMSE between viscosity predictions (from
913 eq. S1) and measurements in training, validation and testing data subsets. 3,000 neural
914 networks with randomly selected architectures were selected and trained to obtain those
915 results. The effects of the numbers of (**a**) compositions in the training data subset, (**b**) hidden
916 activation units, (**c**) hidden layers, (**d**) number of activation units per layer, and of the dropout
917 probability (**e**) were explored. Subplot (c) is a violin plot with extreme values showed. Subplots
918 (b), (d) and (e) are scatter plots in which each slightly transparent symbol corresponds to a
919 given neural network; less transparency is directly indicative of a higher number of models for a
920 given X-Y value.

921 **Figure 4.** Prediction examples: (**a**) Melt viscosity can be predicted using various theories with a
922 great accuracy, as shown by examples highlighting the good match between measurements
923 (symbols) and model (curves) predictions from the Adam-Gibbs and Free Volume theories
924 (Supplementary Materials); (**b**) Structural investigation are made through Raman spectra

925 predictions, which compare well with experimental data for albite and sodium trisilicate glasses
926 for instance.

927 **Figure 5:** Comparison between predicted and measured viscosity in the Na₂O-K₂O-Al₂O₃-SiO₂
928 system. Predictions can be made using theories like Adam-Gibbs (**a**, eq. 1) and free volume (**b**,
929 eq. 2), or empirical equations like MYEGA (**c**, eq. 5), Avramov-Milchev (**d**, eq. 4), and Tamman-
930 Vogel-Fulcher (**e**, eq. 3). See table 3 for RMSE.

931 **Figure 6:** Comparison between (**a**) predicted glass transition temperatures and those calculated
932 from undercooled viscosity data, when available, (**b**) $S^{conf}(T_g)$ values from (Richet, 1984; Neuville
933 and Mysen, 1996; Neuville, 2006; Le Losq and Neuville, 2013, 2017; Le Losq et al., 2014, 2017),
934 (**c**) density, (**d**) refractive index, and (**e**) R_{Raman} . See table 3 for RMSE.

935 **Figure 7:** Glass fragility versus melt $C_p^{conf}(T_g)/S^{conf}(T_g)$ ratio. Symbols are predictions of the deep
936 learning framework on the different subsets of the $D_{viscosity}$ dataset. The dashed line is the
937 relationship observed by Webb (2008, abbreviated W2008 in the figure) using experimental
938 heat capacity data, and the dotted line is that observed by Russell and Giordano (2017,
939 abbreviated RG2017 in the figure). Except two extreme outliers that corresponds to Al₂O₃-SiO₂
940 melts with more than 30 mol% Al₂O₃, a general good agreement is observed.

941 **Figure 8:** Melt and glass properties vary in a complex way with glass network topology. i-Melt
942 reveals that parameters such as (**a**) the viscous glass transition temperature T_g and (**b**) B_{FV} , an
943 activation energy term in the Free Volume theory (eq. 2), strongly vary depending on R_{Raman} .
944 Other terms also show more complex variations, influenced by cationic mixing interactions and
945 steric hindrance effects, such as the glass configurational entropy $S^{conf}(T_g)$ (**c**) or the free volume

946 parameter C_{FV} (**d**). Each symbol represents the calculation for a randomly generated
947 composition (n=10,000) in the glass-forming domain of the $\text{Na}_2\text{O}-\text{K}_2\text{O}-\text{Al}_2\text{O}_3-\text{SiO}_2$ system (Fig. 1).

948 **Figure 9:** Spearman correlation matrix between the different variables predicted by i-Melt or
949 calculated from those predictions. The large the circles, the larger the correlation. A correlation
950 of 1 or -1 means a perfect monotonic (possibly non linear) correlation. Correlations were
951 calculated from the predictions for the 10,000 randomly generated composition in the glass-
952 forming domain of the $\text{Na}_2\text{O}-\text{K}_2\text{O}-\text{Al}_2\text{O}_3-\text{SiO}_2$ system (Fig. 1).

953 **Figure 10:** High temperature viscosity limit. (**a**) histograms of the high temperature viscosity
954 limits A_{TVF} , A_e , A_{FV} and A_{AM} predicted for 10,000 melt composition randomly selected from the
955 glass-forming domain of the $\text{Na}_2\text{O}-\text{K}_2\text{O}-\text{Al}_2\text{O}_3-\text{SiO}_2$ system. (**b**) A_e versus $\text{Al}/(\text{Al}+\text{Si})$ diagram
956 highlighting a possible compositional dependence of A_e . The ternary diagram shows again the
957 randomly selected compositions.

958 **Figure 11:** Configurational entropy at T_g , $S^{conf}(T_g)$, of melts in the upper part ($\text{SiO}_2 > 50$ mol%) of
959 the $\text{K}_2\text{O}-\text{Na}_2\text{O}-\text{Al}_2\text{O}_3-\text{SiO}_2$ system. $S^{conf}(T_g)$ vary non-linearly with oxide contents in the ternary
960 diagrams (**a**) $\text{Na}_2\text{O}-\text{Al}_2\text{O}_3-\text{SiO}_2$ and (**b**) $\text{K}_2\text{O}-\text{Al}_2\text{O}_3-\text{SiO}_2$. In silicate melts (**c**), a mixed alkali effect
961 (MAE) is observed upon Na-K mixing. It disappears as $[\text{Al}]/[\text{Na}+\text{K}]$ increases (**d**, **e**, **f**). Al
962 enrichment generally lead to decreasing $S^{conf}(T_g)$, and minimizing the MAE. Al- and K-rich melts
963 thus present low $S^{conf}(T_g)$.

964 **Figure 12:** Melt fragility, m , of melts in the upper part ($\text{SiO}_2 > 50$ mol%) of the $\text{K}_2\text{O}-\text{Na}_2\text{O}-\text{Al}_2\text{O}_3-$
965 SiO_2 system. Fragility is represented in the upper part of the ternary sodium (**a**) and potassium
966 (**b**) aluminosilicate systems, as well as as a function of the silica fraction and the potassium to

967 total alkali ratio of silicate, peralkaline and tectosilicate melts (**c, d, e, f**). No MAE is observed on
968 melt fragility, which depends largely on melt silica content.

969 **Figure 13:** Deep learning framework predicted variations in (**a,b**) glass transition temperature
970 T_g , (**c,d**) relative density and (**e,f**) refractive index at 589 nm in the upper part ($\text{SiO}_2 > 50 \text{ mol\%}$)
971 of the ternary Na (left) and K (right) aluminosilicate systems.

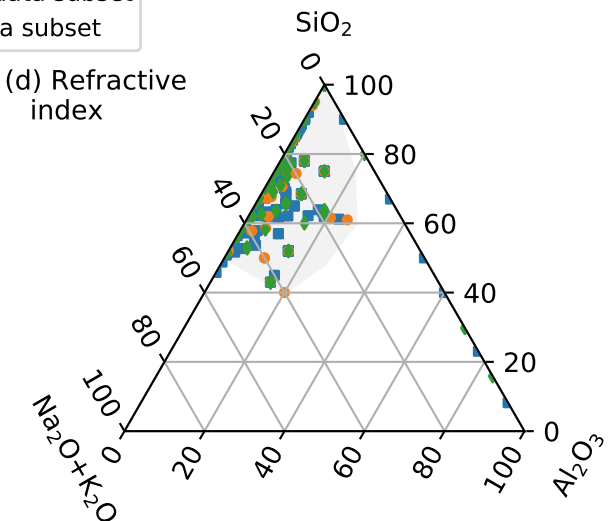
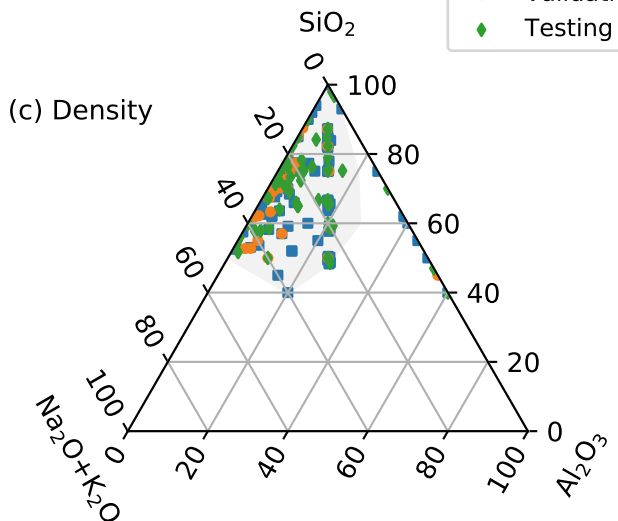
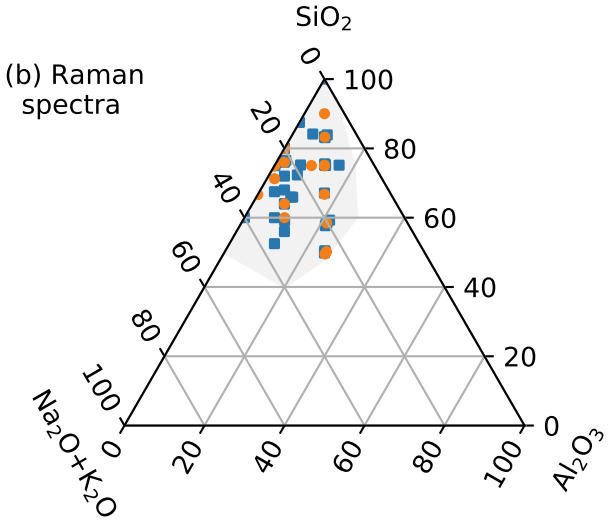
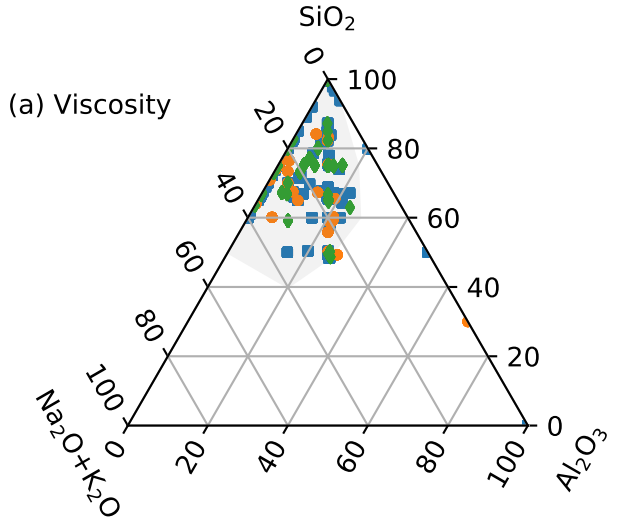
972 **Figure 14:** (**a**) structural R_{Raman} and (**b**) configurational entropy maps as a function of the ratio
973 $\text{K}/(\text{K+Na})$ and the rheological agpaitic index, calculated as $(\text{Na}_2\text{O} + \text{K}_2\text{O} + \text{CaO} + \text{MgO} +$
974 $\text{FeO})/(\text{Al}_2\text{O}_3 + \text{Fe}_2\text{O}_3)$. On top of the maps, symbols of rhyolite effusive (red circles) and
975 explosive (black squares) eruptions from Di Genova et al. (2017) are represented. Some scatter
976 in the maps is visible during transitions, it originates from some model noise and the fact that
977 the color transitions are numerically sharp.

978

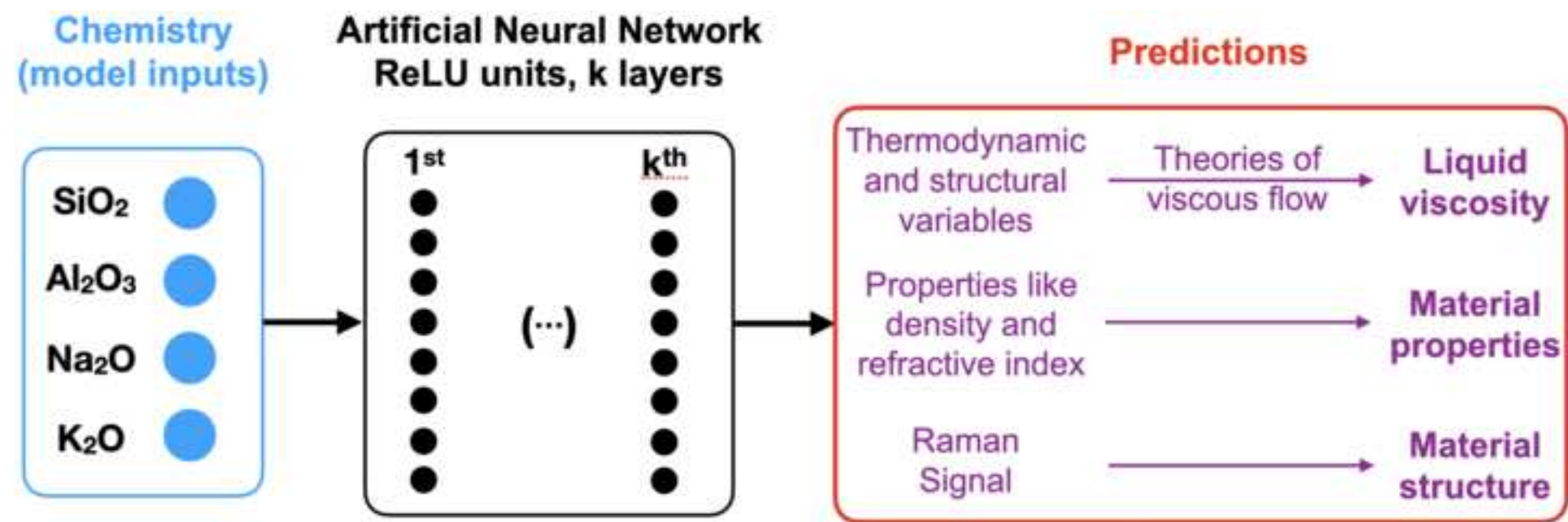
979

Figure 1

Click here to
access/download;Figure;Figure1_TernaryData.pdf



- Glass-forming domain
- Training data subset
- Validation data subset
- ◆ Testing data subset



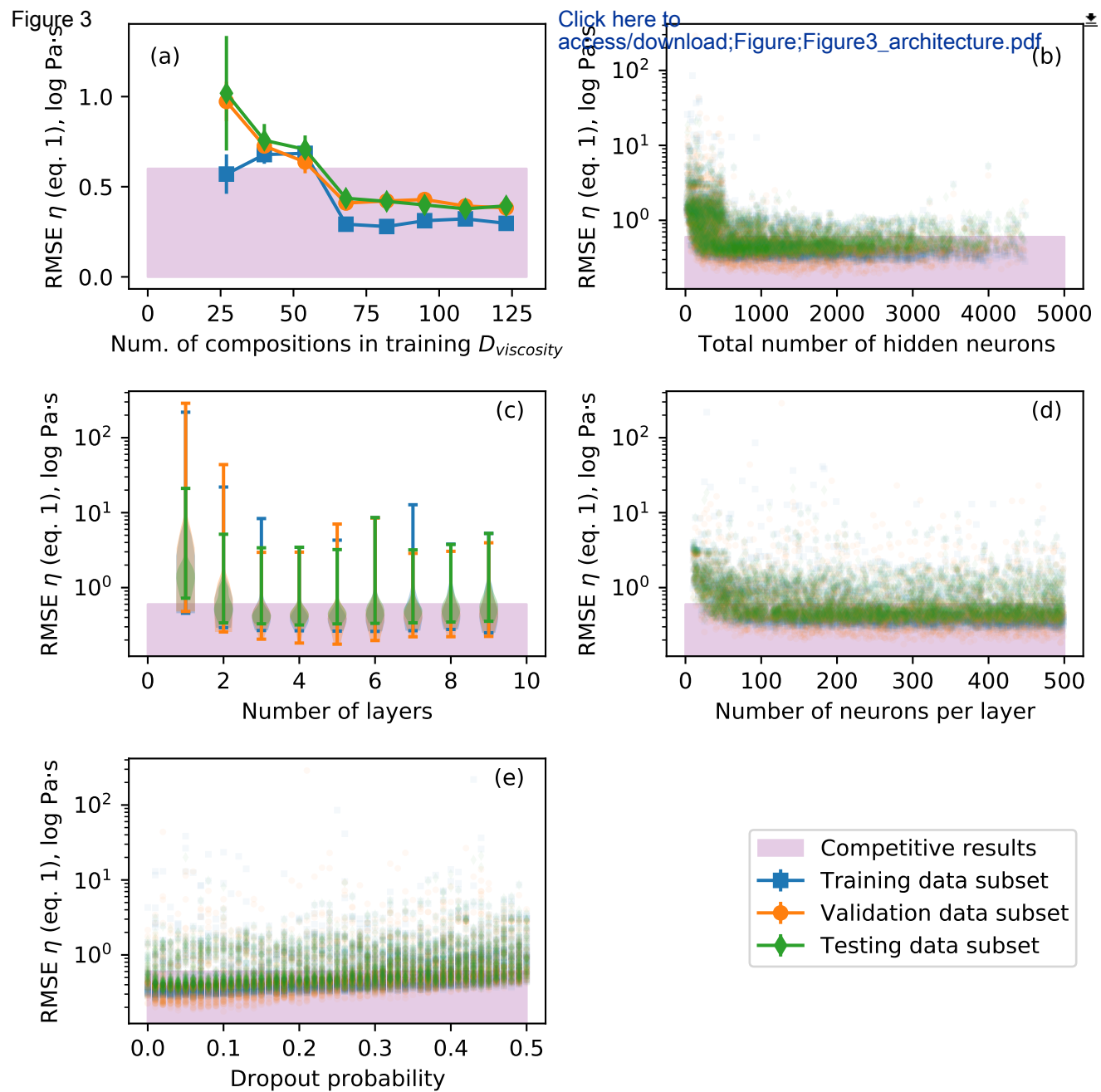
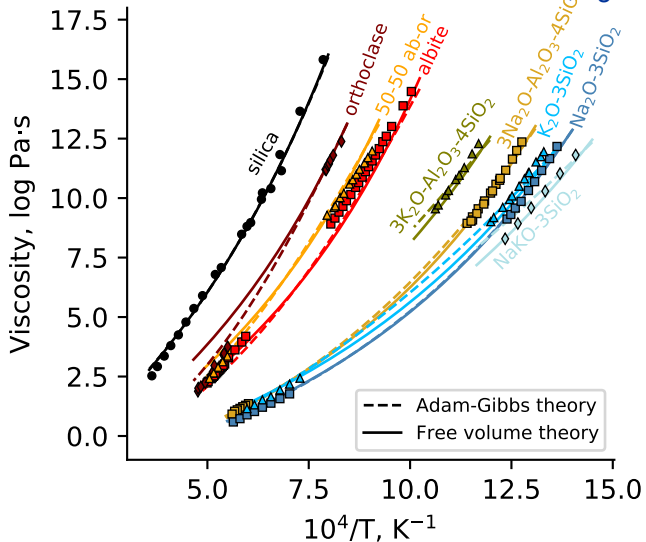


Figure 4

(a) melt mobility
Click here to
access/download; Figure; Fig

(b) glass Raman signals

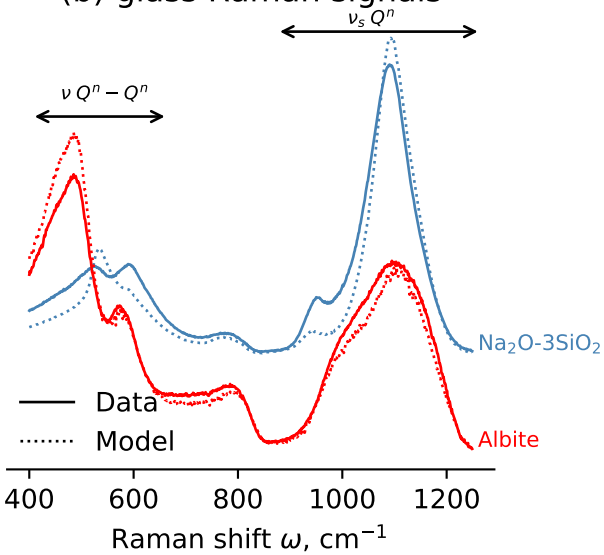
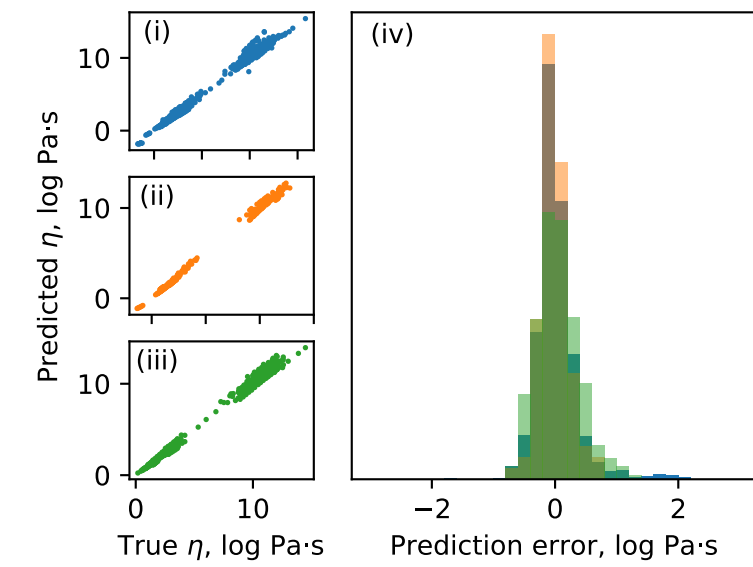


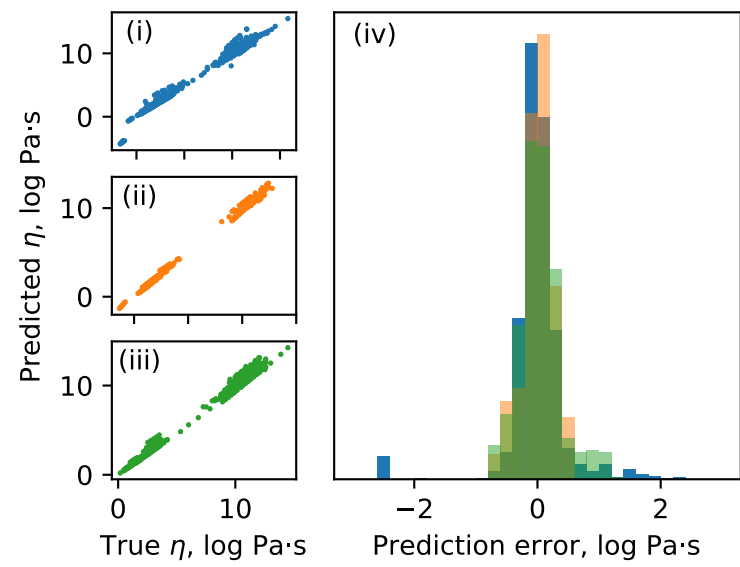
Figure 5

[Click here to access/download;Figure;Figure5_compvisco.pdf](#)

(a) Adam-Gibbs (AG)

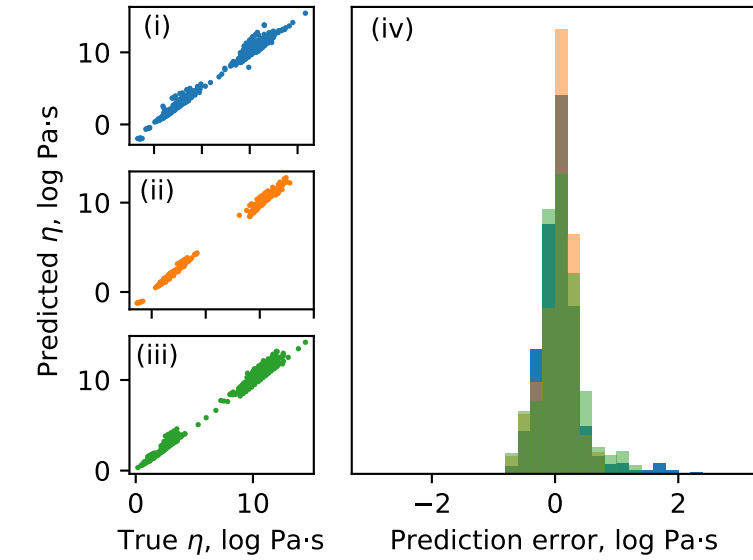


(b) Free Volume (FV)

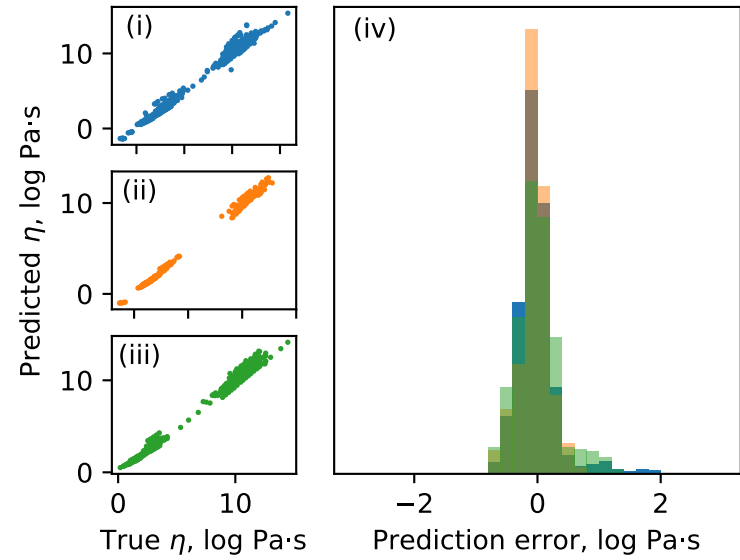


Training subset
Validation subset
Test subset

(c) MYEGA



(d) Avramov-Milchev (AM)



(e) TVF

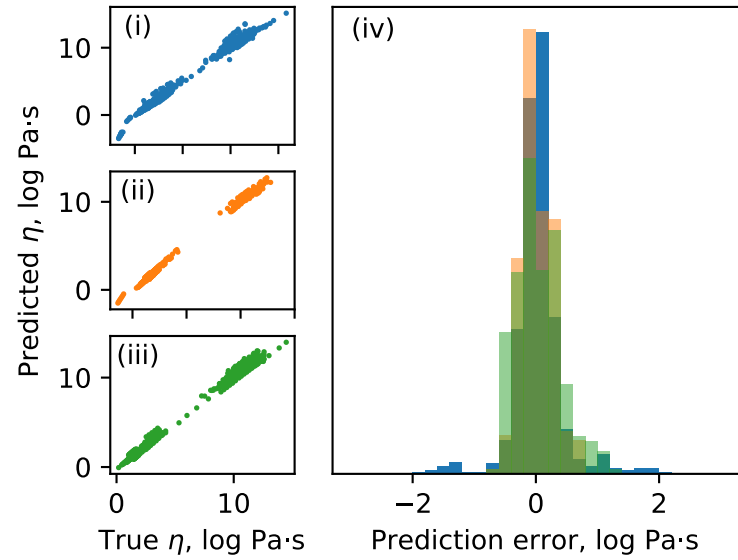
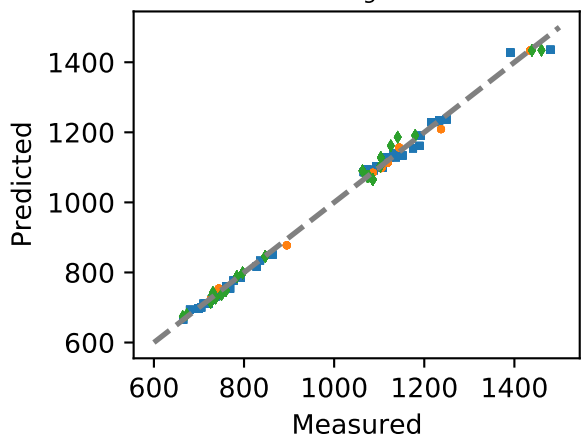
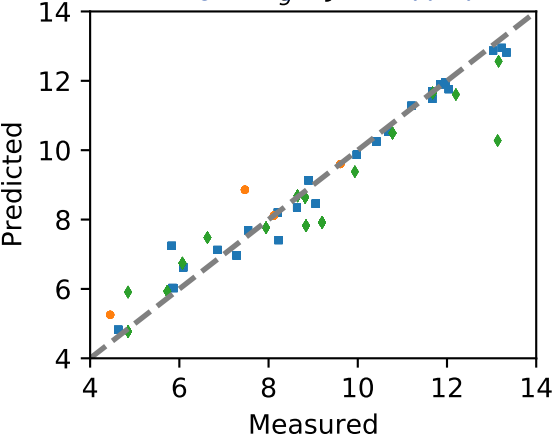
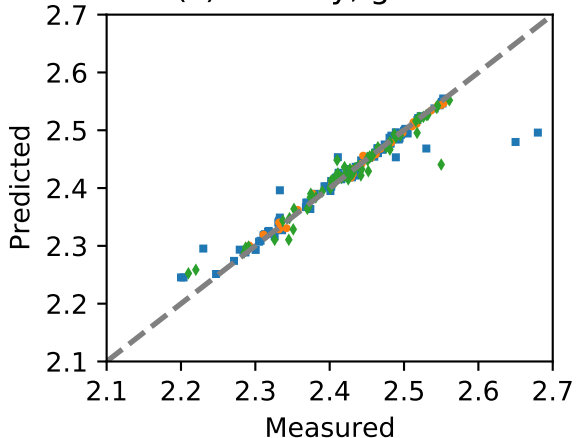
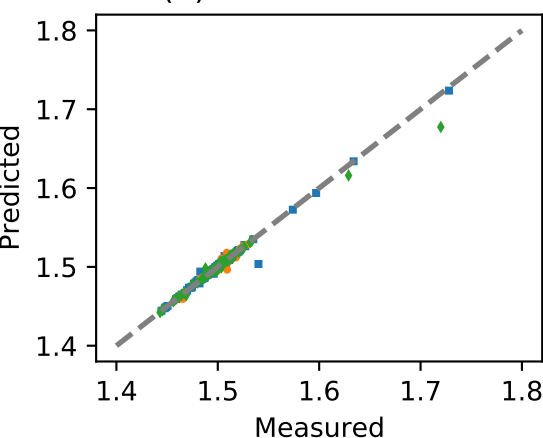
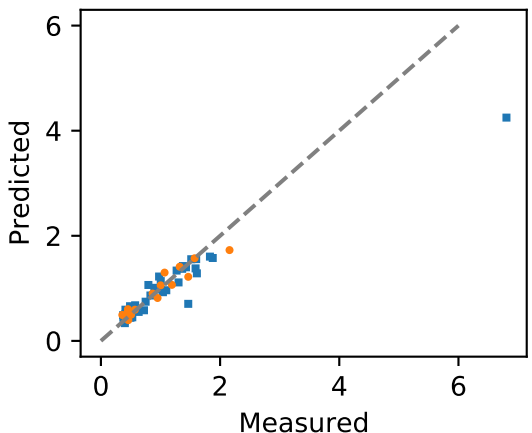


Figure 6

(a) T_g , KClick here to
access/download (a); Figure 6 properties(b) $S_{conf}(T_g)$ J mol $^{-1}$ K $^{-1}$ (c) Density, g cm $^{-1}$ 

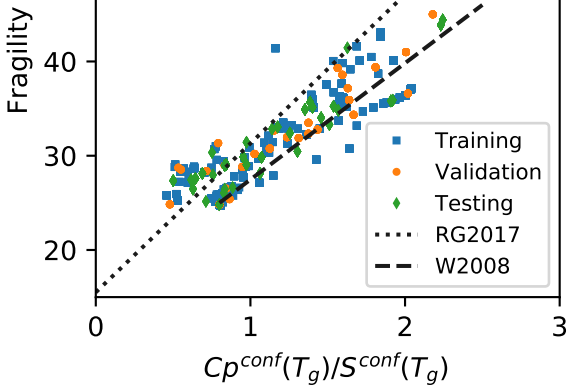
(d) Refractive index

(e) R_{Raman} 

- Training
- Validation
- ◆ Testing
- 1:1

Figure 7

[Click here to access/download;Fig](#)



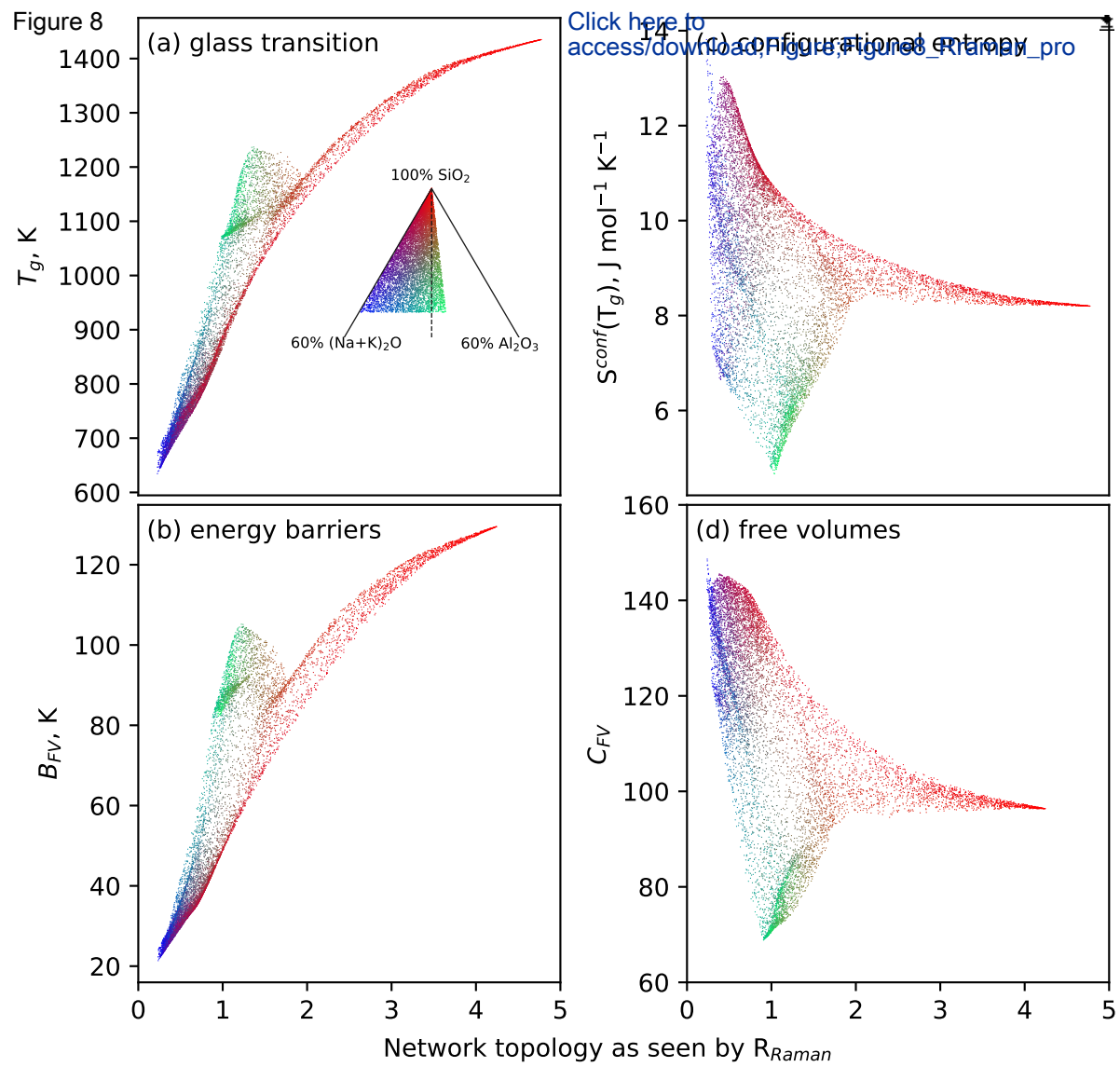


Figure 9 R_{Raman}

[Click here to access/download Figure_Figure9_correlations.pdf](#) - 1

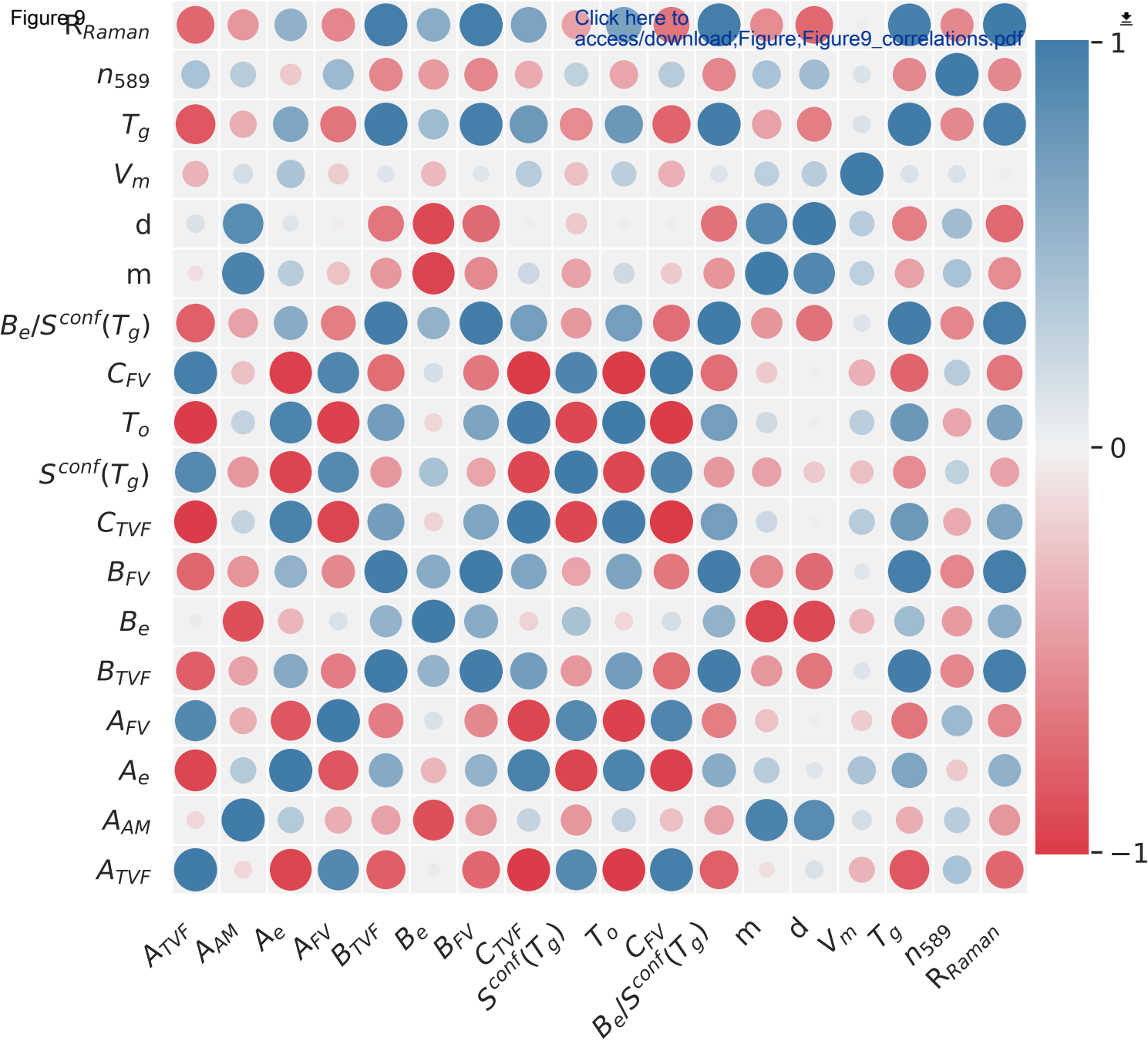


Figure 10

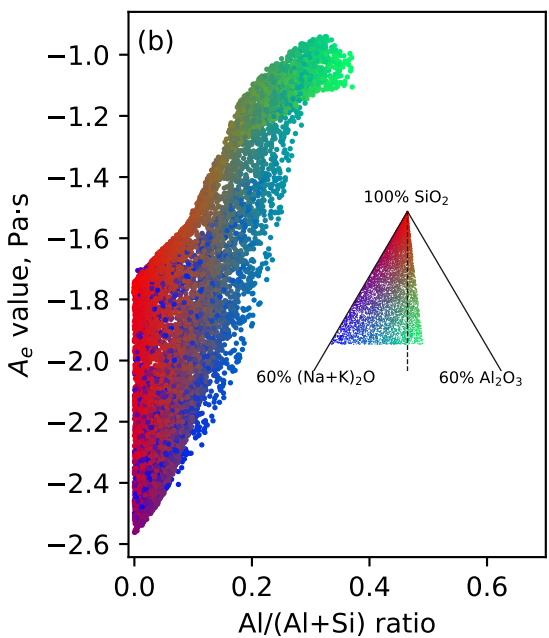
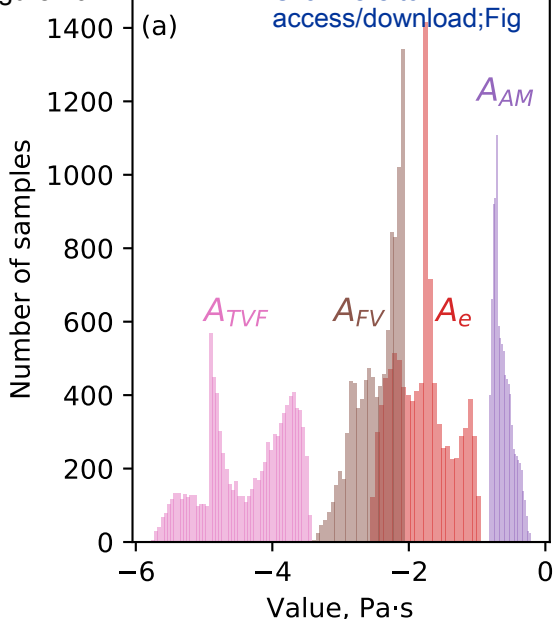
[Click here to access/download;Fig](#)

Figure 11

[Click here to access/download/Figure;Figure11_entromaps.pdf](#)

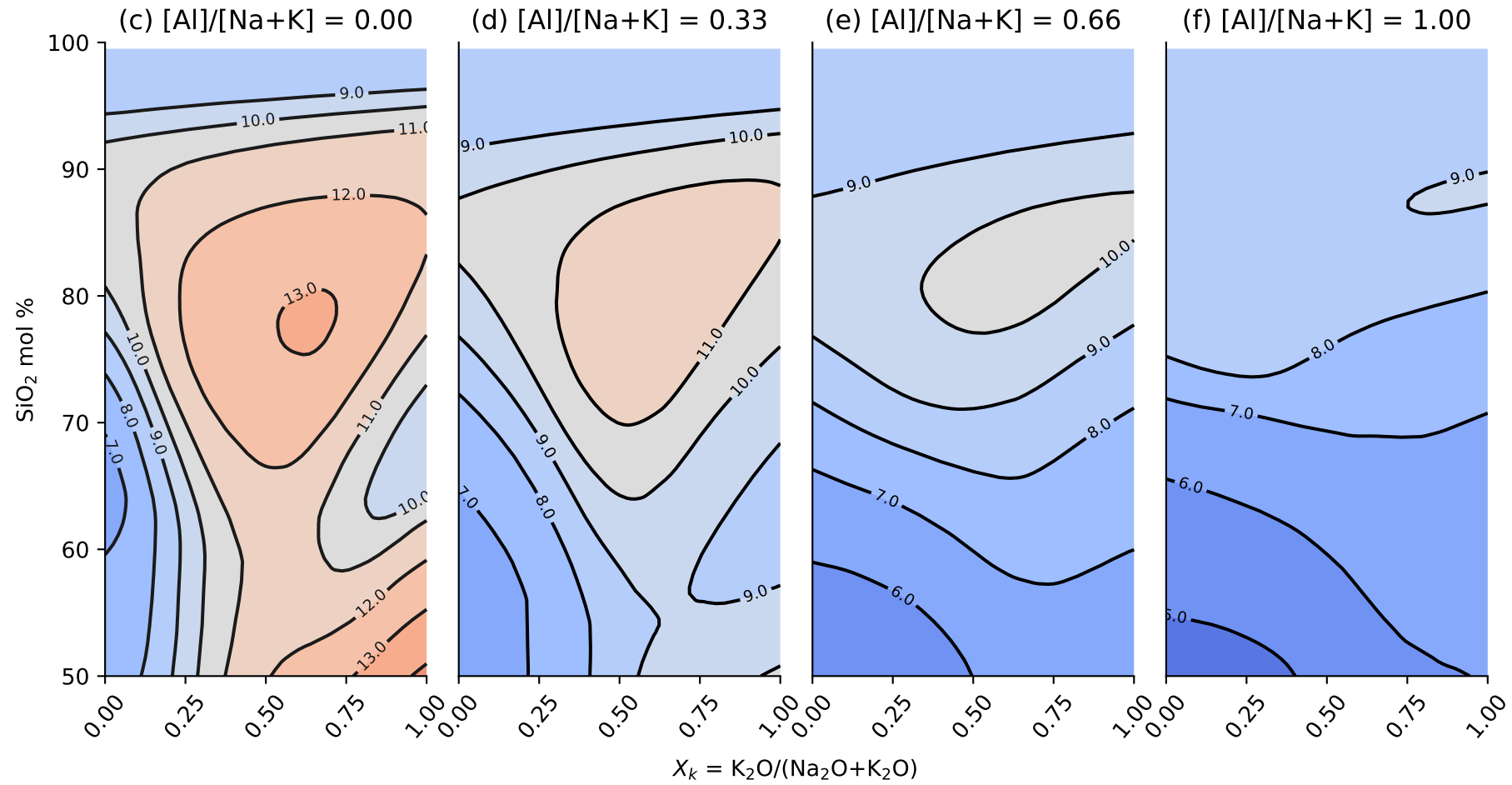
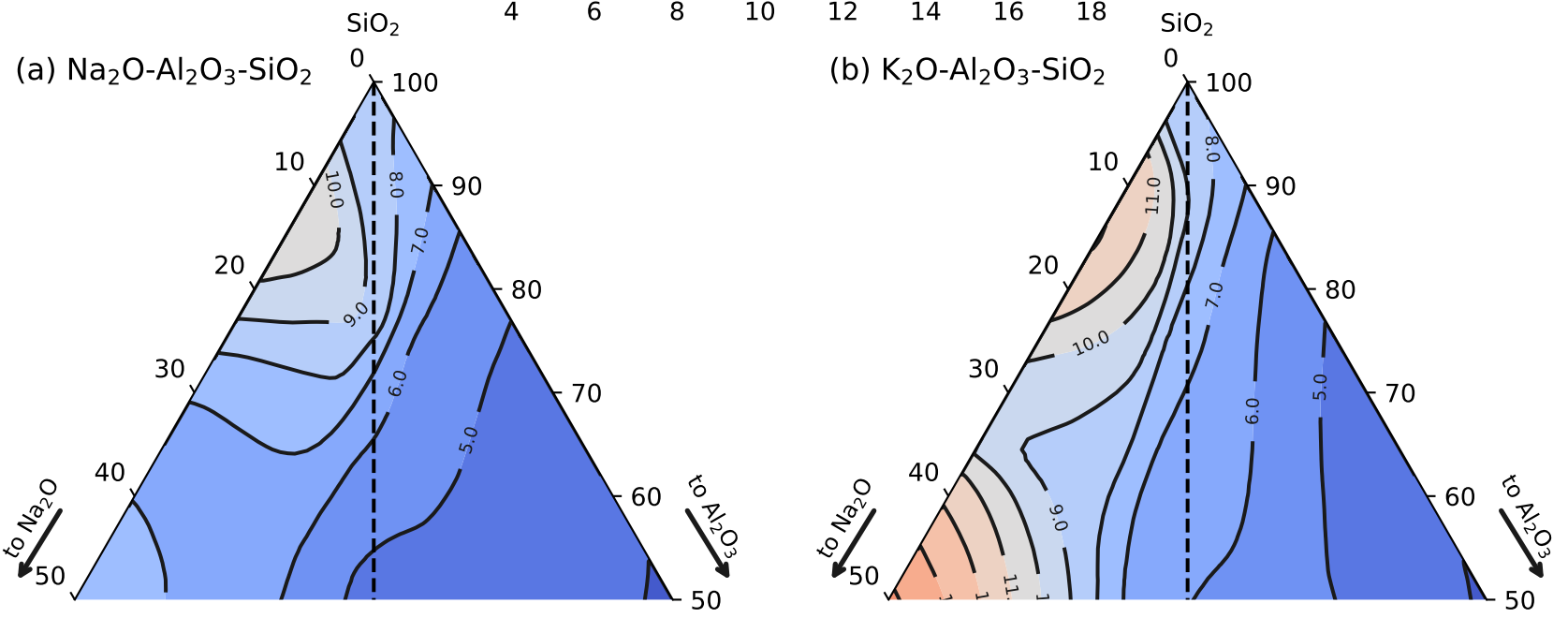


Figure 12

Fragility

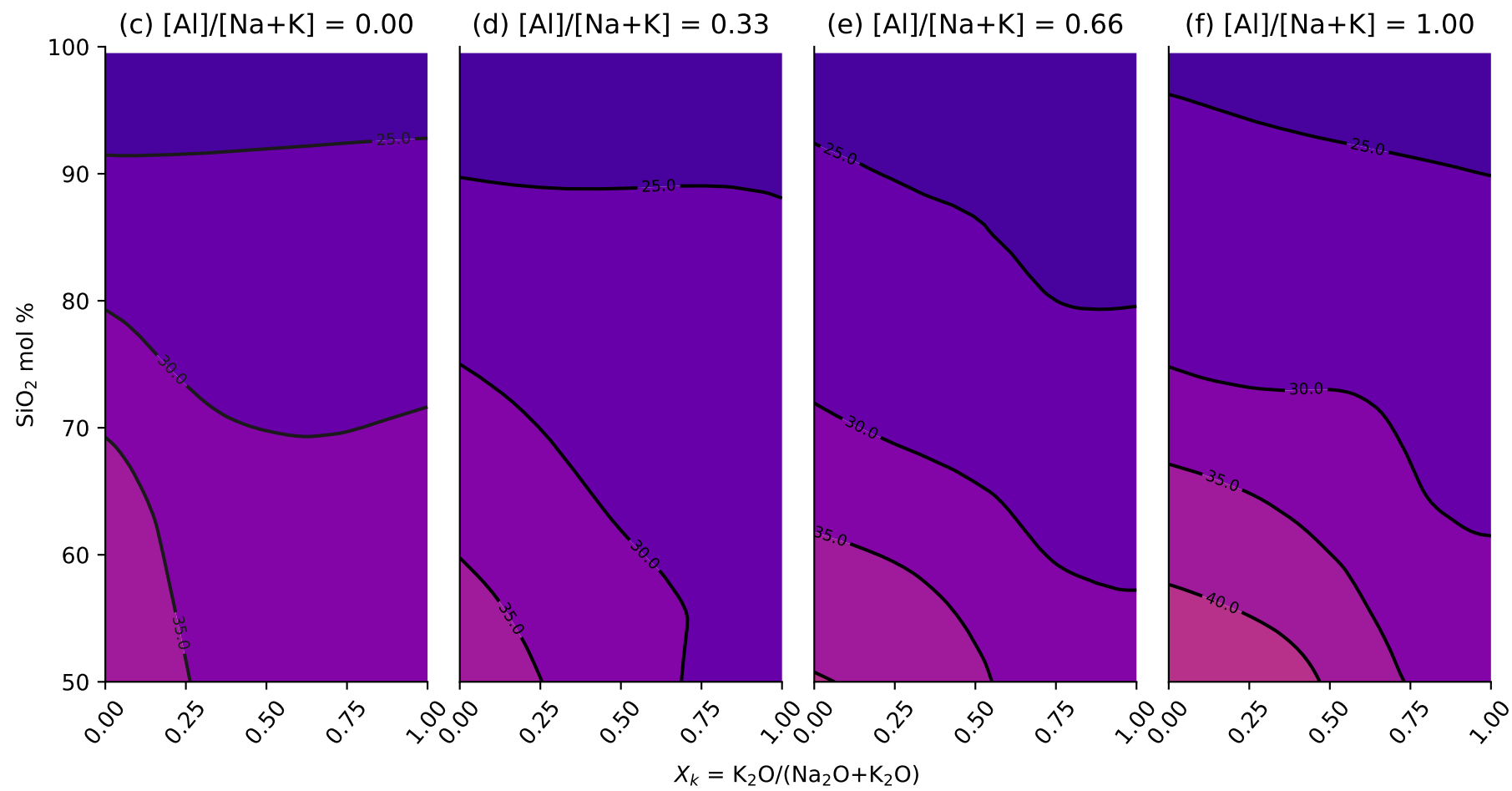
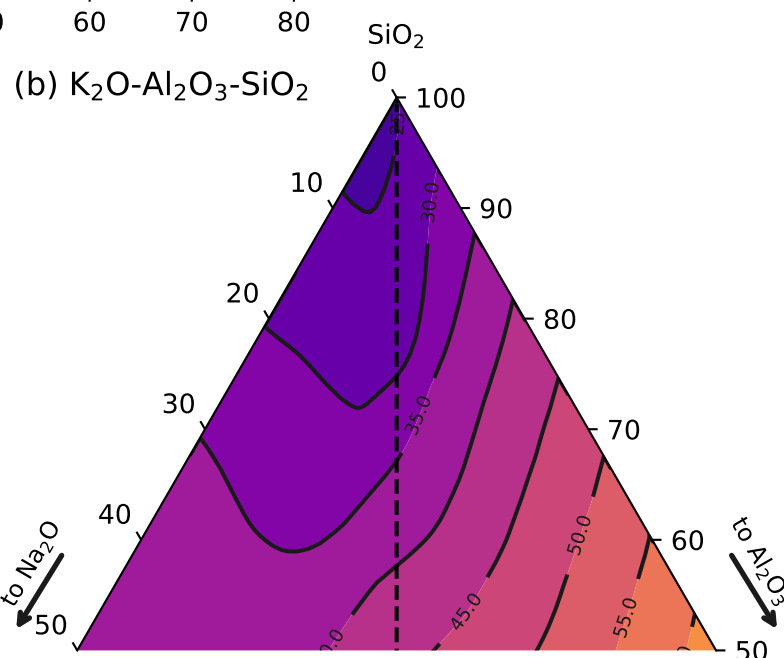
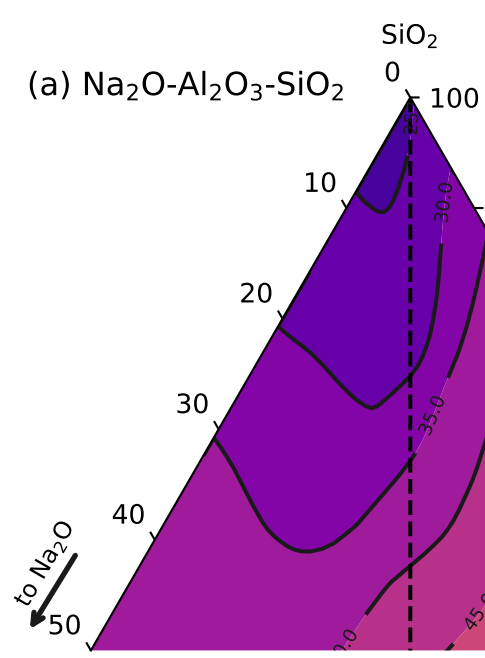
[Click here to access/download;Figure;Figure12_Fragility.pdf](#)

Figure 13

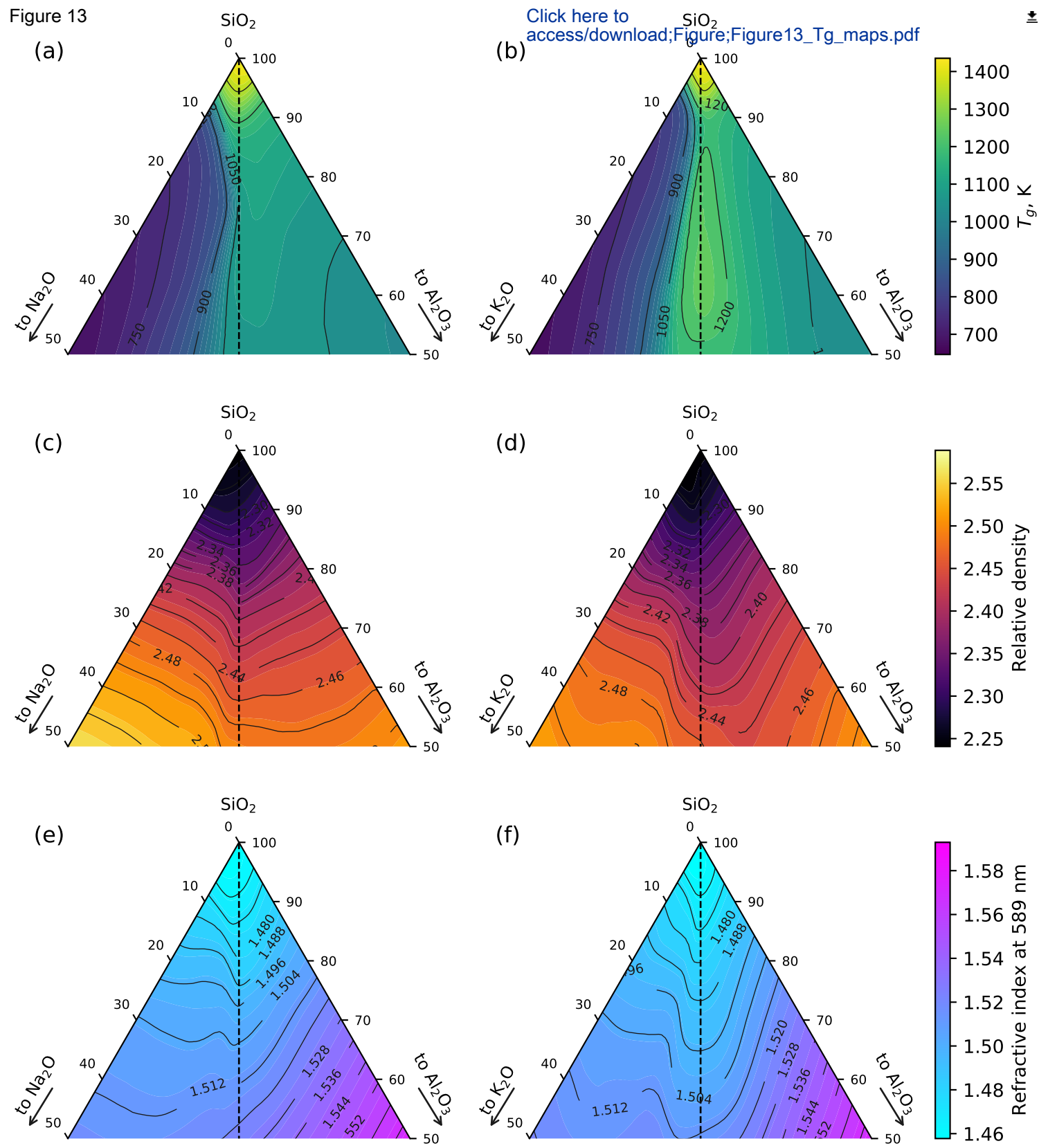
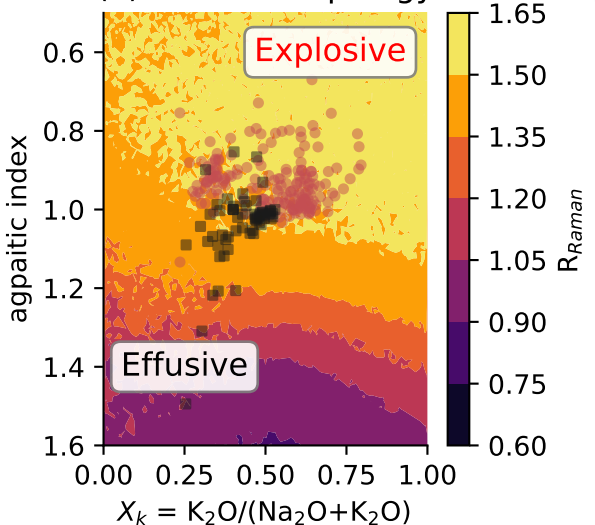
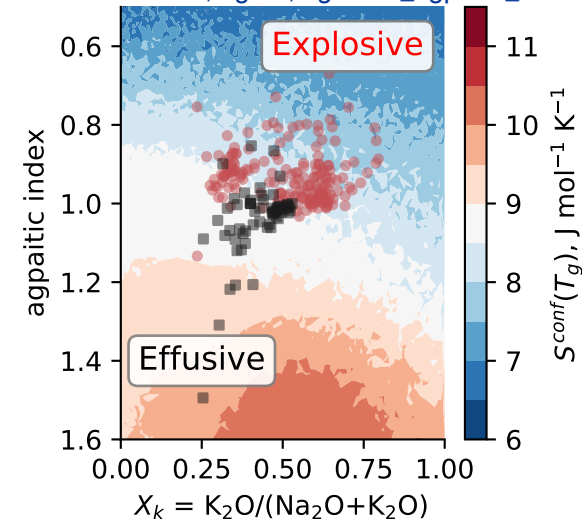


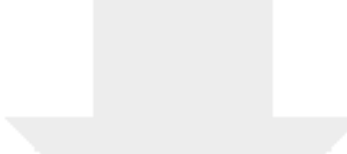
Figure 14

(a) Network topology



(b) Configurational entropy





Click here to access/download
Electronic Annex
i-MELT_DevVersion.zip



Declaration of interests

The authors declare that they have no known competing financial interests or personal relationships that could have appeared to influence the work reported in this paper.

The authors declare the following financial interests/personal relationships which may be considered as potential competing interests:

